Title: Nanoscale indentation of plasma membrane establishes a contractile actomyosin scaffold through selective activation of the Amphiphysin-Rho1-Dia/DAAM and Rok pathway

Authors: Tushna Kapoor [ORCID 0000-0001-6003-8535], Pankaj Dubey [ORCID 0000-0001-7532-8332][a], Seema Shirolikar, and Krishanu Ray [ORCID 0000-0001-6406-3199]*

Department of Biological Sciences, Tata Institute of Fundamental Research, Mumbai 400005, India.

*-Address for correspondence: Krishanu Ray, DBS, TIFR, Mumbai 400005, India. E-mail: krishanu@tifr.res.in, krishanu64@gmail.com, Phone: +91-22-22782730, Fax: +91-22-2280-4610/11.

a- Current address: Blizard Institute, Barts and The London School of Medicine and Dentistry, Queen Mary University of London, 4 Newark Institute, E1 2AT, UK.

Highlights:

- Stretching the plasma membrane around a spermatid head recruits Amphiphysin and Rho1.
- Rho1 activation triggers F-actin assembly *in situ* through Diaphanous and DAAM.
- Rho1-Rok activation assembles actomyosin scaffold around the folded plasma membrane.
- Contractile actomyosin enables plasma membrane to clamp onto the spermatid head.

Author summary:

Sperm released from the somatic enclosure is essential for male fertility. During differentiation, the somatic cell membrane, associated with dense F-actin scaffold, tightly hold each spermatid head before release. Kapoor et al., showed that the bending and stretching of the plasma membrane trigger the assembly of an actomyosin scaffold around the bent membrane, which clamps the spermatids together preventing the premature release and somatic cell penetration. This finding provides new insight into the molecular networks activated by mechanical bending of the plasma membrane.

Abstract:

Nanoscale bending of plasma membrane increases cell adhesion, induces cell-signalling, triggers F-actin assembly and endocytosis in tissue-cultured cells. The underlying mechanisms are not very well understood. Here, we show that stretching the plasma membrane of somatic cyst cell around rigid spermatid heads generates a stable, tubular endomembrane scaffold supported by contractile actomyosin. The structure resembles an actin-basket covering the bundle of spermatid heads. Genetic analysis suggests that the actomyosin organisation is nucleated exclusively by the Formins, Diaphanous and DAAM, downstream of Rho1, recruited by the Bin-Amphiphysin-Rvs (BAR)-domain protein, Amphiphysin, around the spermatid heads. Actomyosin activity at the actin-basket gathers the spermatid heads into a compact bundle and resists the invasion of the somatic cell by the intruding spermatids. These observations revealed a new response mechanism of nanoscale bending of the plasma membrane, which generates a novel cell adhesion strategy through active clamping.

Keywords: Actomyosin, Amphiphysin, Diaphanous, Rho-1, Rho-kinase, Spermiation, *Drosophila*

Glossary: TE - Terminal epithelium, HCC - Head cyst cell, TCC - Tail cyst cell, NB - Nuclei bundle/Spermatid head bundle, Caplet and Basket - parts of Actin cap, SJs - Septate Junctions, CC-coiled cyst.

46 **Introduction:**

47 The plasma membrane is the ultimate barrier in eukaryotic cells. It also acts as a mechanical force
48 sensor and can withstand severe distortions (Pontes et al., 2013) and indentation up to a few microns
49 by nano-sized objects (Yang and Saif, 2007). Nanoscale deformation of the cell membrane increases
50 cell adhesion to the substrate (Viswanathan et al., 2015), and confers cell fate and induces osteogenic
51 differentiation of mesenchymal stem cells (Abagnale et al., 2015). It is also suggested that some
52 viruses are likely to exploit this property to invade the host cell (Wiegand et al., 2020). Therefore,
53 understanding the mechanism of cellular response to plasma membrane indentation is critical to
54 identify the determinant factors.

55 Nanoscale bending of plasma membrane acts as hotspots for clathrin-dependent endocytosis
56 (Zhao et al., 2017), which is likely to signal the cell and provide access to pathogens. The bending of
57 the plasma membrane due to the tight wrapping of ~100 nm diameter nanopillars is sensed by
58 Clathrin, which induces dynamin-mediated endocytosis (Zhao et al., 2017). On the other hand, the
59 bending of the basolateral cell membrane around nanopillars of diameters ~100-400 nm triggers local
60 F-actin assembly through the recruitment of Formin-Binding-Protein-17 (FBP-17) and Arp2/3
61 activation (Lou et al., 2019). Thus, molecular response to nano-indentation of the plasma membrane
62 appears to depend on the surface topography. The underlying mechanism is, however, not
63 investigated. Moreover, all these studies are carried out *in vitro* using synthetic conditions. Hence,
64 these conjectures and their biological relevance are yet to be established *in vivo*.

65 In *Drosophila* testis, 64 spermatids mature synchronously within a somatic cell enclosure
66 formed by the head-cyst-cell (HCC) and tail-cyst-cell (TCC) that are held together by septate junction
67 (SJ) proteins (Dubey et al., 2019). Each mature spermatid head is a rigid, ~10 µm long rod of ~200 nm
68 diameter. As the cyst matures, it moves through the terminal epithelium (TE) region at the base of the
69 testis until mature spermatids are released from the cyst enclosure, and progress into the seminal
70 vesicle (SV) (Dubey et al., 2016). During this last stage, spermatid heads push against the plasma
71 membrane of the HCC and an actin-rich structure (actin cap), contributed by the somatic cyst cell,
72 appeared to hold the spermatid heads and prevent premature release by rupturing the HCC (Desai et
73 al., 2009; Dubey et al., 2016). Actin cap is composed of two distinct domains that are clearly separated
74 from each other - a relatively stable actin-rich 'basket' domain envelopes the sperm head bundle,
75 whereas the 'caplets' form around the HCC membrane whenever a sperm head intrudes beyond 2 µm
76 from its resting position (Dubey et al., 2016). Every attempt of a spermatid head intrusion is
77 immediately repulsed by transiently assembled caplets which are formed by the WASp-Arp2/3-
78 dependent process around the indented plasma membrane of the HCC (Dubey et al., 2016). The caplet

79 disappears as soon as the intruding spermatid head reverts to its initial position. The mechanism of
80 the basket assembly, which persists even after the spermatid release, was not explored.

81 Here, we provide a comprehensive sub-cellular and molecular-genetic evaluation of the
82 basket assembly that helped to derive a novel clamping mechanism. We find that the basket is
83 composed of a highly tubular membrane scaffold supported by actomyosin. It is assembled exclusively
84 through concerted activities of the Rho1 GTPase, and the formins Diaphanous and DAAM. The Bin-
85 Amphiphysin-Rvs (BAR) domain protein, Amphiphysin, possibly recruits Rho1/RhoA at the basket.
86 Rho1 recruits and activates nonmuscle myosin-II through Rho-kinase. The actomyosin activity
87 maintains the integrity of the actin-basket and holds the spermatid heads together in a parallel bundle,
88 which is essential for maintaining male fertility (Dubey et al., 2019). Basket domain also prevents the
89 penetration of the somatic cell by spermatid heads. Together, these results describe an
90 unprecedented role of membrane bending in triggering the assembly of an actomyosin clamp at the
91 plasma membrane. We postulate that the bending of the HCC plasma membrane around spermatid
92 heads triggers the recruitment of specific BAR domain proteins to initiate the basket assembly, and
93 discuss the significance of these findings in the context of wound healing and tissue morphogenesis.

94

95 **Results:**

96 **Actin-Basket consists of extensively tubular endomembrane and F-actin**

97 The cysts containing coiled spermatids, with characteristic compacted NBs (Fig 1A; arrows, Fig 1B) are
98 found within the TE zone. During the initial stage of individualisation, F-actin cones (Investment Cones
99 – IC) consisting of dendritic actin form around each spermatid head (arrowhead, Fig 1B; Fig S1A), and
100 move down the tail (Noguchi and Miller, 2003). As the ICs progressed, the spermatid heads were
101 rearranged in a parallel bundle (Nuclei Bundle – NB, Fig S1B-E), and a different type of F-actin
102 structure, called actin cap (Desai et al., 2009), appears inside the HCC around the NB (yellow
103 arrowheads, Fig S1C-E). Actin cap consists of a dense F-actin basket and multiple caplet domains
104 (Dubey et al., 2016) (arrowhead and arrow, Fig S1F). The basket is most pronounced in the middle
105 region of the TE, which had fully coiled spermatid tails (arrowhead, Fig S1F).

106 To get a more comprehensive understanding of the actin cap, which is formed inside the HCC
107 (Desai et al., 2009), we used a combination of confocal and Structured Emission Depletion (STED)
108 microscopy. We used *PpYGal4*, which expresses at a relatively higher level in the HCC during the
109 terminal stage of spermatid differentiation. The *PpY>GFP-utr* expression marked caplets (arrows, Fig
110 1C-C'), as well as a dense F-actin basket, surrounding the NB (arrowheads, Fig 1C-C'). In addition, we

111 noted F-actin sleeves around individual spermatids (open arrows, Fig 1C-C'), henceforth referred to as
112 'actin sleeves'. The actin sleeves present in between each spermatid head in an NB were also
113 prominent in the STED images (open arrows, Fig 1D-D'''). The caudal part of the actin sleeves, marked
114 by Phalloidin, but not by GFP-Utr (dashed open arrow, Fig 1C-C'; open arrows, Fig 1D''-D''') are most
115 likely contributed by the TCC, since mature sperms released into the SV do not stain for F-actin.

116 As described earlier (Tokuyasu et al., 1972b), Transmission Electron Microscopy (TEM) of
117 transverse sections of NBs indicated that individual spermatid heads are tightly wrapped by the HCC
118 membrane (arrows, Fig 1E). The HCC membrane is highly tubulated at the rostral end of the spermatid
119 heads (arrowheads, Fig 1E), which are buried deep into the HCC. The membrane tubules also had
120 bulbous termini (arrowheads, Fig 1F-G), and electron-dense material coated the membrane buds
121 (arrowhead, Fig 1F). These structural features resembled the tubulobulbar-complex found around
122 spermatid heads inside Sertoli cells in mammalian testis (Guttman et al., 2004). Such tubules were not
123 detected near the HCC-TCC interface (arrows, Fig 1H), which is held together by SJs (Dubey et al.,
124 2019). Together, these analyses indicated that each spermatid is tightly sleeved with the somatic cell
125 membrane supported by F-actin (actin sleeve), and the head bundle (NB) is surrounded by a highly
126 tubular actin-rich membrane, which we redefine as the 'basket' domain (Fig 1A") (Video S1).

127 The baskets were classified in two categories - *mature* baskets with distinctively rich Phalloidin
128 staining (Fig 1C; S1F), and relatively *thin* ones with barely detectable Phalloidin staining surrounding
129 the NB (Fig S1G-G'). These two morphological classes were also distinguished by significantly different
130 F-actin volume (Fig S1H). Altogether, these observations indicated that the basket domain forms
131 around the spermatids heads as the coiled spermatids progress into the TE.

132 **Basket domain is a contractile structure composed of relatively stable F-actin**

133 *Ex-vivo* time-lapse imaging of *Drosophila* testes expressing *sqh::utr-GFP* and *ProtB-dsRed,* marking the
134 F-actin and the NB, respectively, revealed that the basket periodically contracts and expands along
135 the axis parallel to the NB (Fig 2A; Video S2). To understand the effect of periodic basket contraction,
136 we used high-intensity pulsed IR laser (800 nm) to ablate a part of the basket. Focussing the laser
137 beam in a 0.75 μm^2 (10x10 pixels) area near the edge of the basket region caused an isotropic
138 retraction of F-actin from the centre of the spot (asterisk, Fig 2B, B"). Over time, the F-actin
139 surrounding the NB dispersed (follow arrowheads, Fig 2B) and accumulated at the caplet region
140 (arrow, 30' 56", Fig 2B; Video S3), with concomitant sheering of the NB (Fig 2B'). To ensure that the
141 loss of F-actin from the basket region caused NB disruptions, we ablated a control spot in the HCC
142 cytoplasm, away from the basket (dashed region, Fig 2C-C') using the same laser power. It did not
143 perturb the caplet and the basket (arrows and arrowheads, Fig 2C), as well as the NB organisation (Fig

144 2C'; Video S4). These results suggested that that basket is a contractile structure required for
145 maintaining the spermatid heads in a tight bundle.

146 Further, the Fluorescence Recovery After Photobleaching (FRAP) revealed that the F-actin at
147 the basket domain is composed of stable and dynamic components (Video S5). The post bleach
148 recovery (t= 5.5'' onwards, Fig 2D-D') reached saturation within 100 seconds (Fig 2E). The data were
149 fitted to a single exponential using the Levenberg-Marquardt iteration algorithm, and the maximum
150 recovery was found to be 0.49 ± 0.006, indicating nearly equal amounts of mobile and immobile
151 fractions of F-actin. Hence, nearly 50% of the F-actin at the basket domain appeared to remain stable
152 for a considerable period.

153 We also noted that thin F-actin-rich extensions (actin tubules) occasionally emanate from the
154 basket domain (open arrowheads, Fig S2; Video S6). These structures may contribute to the partly
155 dynamic nature of the basket, and may potentially mark the tubular membrane extensions observed
156 by the TEM (Fig 1E, G).

157 Together, the anatomical data and the time-lapse analyses suggested that a relatively stable
158 membrane-actin assembly around the spermatid heads during the final stages of spermatid
159 maturation maintains them in a tight bundle. We wanted to understand how such a complex and
160 unprecedented structure forms and its biological relevance.

161

162 **Rho1 activation organises the F-actin assembly at the Basket domain**

163 *Drosophila* genome codes for Rho1 (Rho A in mammals), three different Rac isoforms, and a
164 Cdc42 orthologue (www.flybase.org). To understand the molecular mechanism of F-actin assembly in
165 the basket domain, we knocked down, as well as altered the functions of these three classes of Rho
166 GTPases in the cyst cells, using *PpYGal4*. Three quantitative parameters - the number of intact NBs,
167 number of progressed ICs and basket morphology - were used to ascertain the cellular and biological
168 impact of these perturbations. Loss of actin cap disrupts the NB and leads to premature release inside
169 the testis (Desai et al., 2009; Dubey et al., 2016). Therefore, we counted the number of intact NBs at
170 the base of the testes to determine the effects of the tissue-specific perturbations (arrows, Fig 3A).
171 Loss of F-actin assembly during the individualisation stage, preceding the spermatid coiling, affects
172 the IC assembly and progression, and the NB packing (Ghosh-Roy et al., 2005). Therefore, we
173 estimated the number of progressed ICs, to clarify that the effect was restricted to the final stage of
174 sperm maturation. Third, we analysed the basket morphology and volume marked by the Phalloidin
175 staining, as well as the anisotropy of NB packing to understand the effects at the subcellular level.

176 The *PpY>Rho1 RNAi* combination was lethal. Knockdown of Rho1 using the relatively milder
177 *SG18.1Gal4,* survived to the adult stage. The TE region contained mostly disrupted NBs (yellow dashed
178 circle, Fig 3B-B', F) and very few progressed ICs (Fig 3G; arrowheads, Fig S3B). The overexpression of
179 dominant-negative Rho1-N19 using *PpYGal4* reduced the number of intact NBs (Fig 3C-C', F) without
180 affecting the progressed ICs (Fig 3G; arrowheads, Fig S3C). A higher proportion of these NBs was
181 associated with visibly thin or deformed baskets (open arrows, Fig 3I-I'; pie chart), as compared to
182 control (Fig 3H-H'; pie chart). The expression of constitutively-active Rho1-V14 (*PpY>Rho1CA*)
183 increased the number of NBs (Fig 3D-D', F) and the proportion of mature baskets (Fig 3J-J'; pie chart),
184 without altering the number of progressed ICs (Fig 3G; arrowheads, S3D). Similarly, Rho1
185 overexpression (*PpY>UAS Rho1*) significantly increased the fraction of NBs associated with mature
186 baskets (pie chart, Fig 3K), without altering the number of NB (Fig 3E-E', F) and progressed ICs (Fig 3G;
187 arrowheads, Fig S3E). Thus, Rho1 activity is implicated in the F-actin assembly at the basket domain.
188 Finally, Rho1 immunostaining revealed a visible enrichment only at the basket domain, and not at the
189 caplets (arrowhead and arrow, Fig 3L-L'). Together these results indicated that Rho1 localisation and
190 activation at the basket domain are essential for the F-actin assembly.

191 Next, we tested the roles of Cdc42 and Rac1. The *PpY>Cdc42 RNAi* testes were shrunken, with
192 no identifiable mature cysts (Fig S4C-D), suggesting that Cdc42 has a broader role in sperm
193 differentiation. Overexpression of the dominant-negative *Cdc42-L89* significantly increased the
194 average number of intact NBs (Fig S4E, P), but there were no identifiable defects in the basket
195 morphology (Fig S4F-F'). Hence, we ruled out a direct involvement of Cdc42 in the basket assembly.
196 The *Rac1* and *Rac2 RNAi*, as well as the overexpression of the dominant-negative Rac1-N17 and Rac1-
197 L89, respectively, did not change the NB and IC counts (Fig S2). However, we noticed an unusually
198 large number of actin tubules emanating from the basket in the *Rac1 RNAi* and DN backgrounds
199 (yellow arrowheads, Fig S2H-H', L-L'). Also, the Rac1-GFP, expressed from its endogenous promoter,
200 was moderately enriched in and around the basket (arrowhead, Fig S4O-O'). Thus, we concluded that
201 Rac1 is likely to maintain actin tubule dynamics. Together, these results suggested that though Rac1
202 is not directly involved in the basket assembly, it may fine-tune actin-membrane dynamics in the
203 basket.

204 In summary, tissue-specific perturbation of different class of Rho-GTPases in the cyst cells
205 suggested that the basket domain is exclusively formed due to the activation and recruitment of Rho1.
206 These observations also raised two specific questions – whether the recruitment and activation of
207 Rho1 lead to the F-actin assembly at the basket domain and how Rho1 is recruited.

208

209 **Basket is composed of linear F-actin nucleated by the formins - Diaphanous and DAAM**

210 The association of GTP-bound Rho1 activates a sub-group of the formin class of the F-actin nucleation
211 promotion factors (Kuhn and Geyer, 2014). Therefore, to identify the role of formins in the basket
212 assembly, we separately expressed RNAi constructs for all the six formins coded by *Drosophila* genome
213 (Breitsprecher and Goode, 2013), *viz.*, Diaphanous (Dia), Dishevelled Associated Activator of
214 Morphogenesis (DAAM), Formin-like (Frl), Formin 3 (Form 3), Formin homology-2 domain-containing
215 (Fhos) and Cappuccino (Capu), using *PpYGal4*. The *dia RNAi* expression led to a severe loss of NBs (Fig
216 4B-B', D) with no significant change in the number of progressed ICs (Fig 4E; S5B). We also noticed a
217 large number of free spermatid heads in the TE in *dia RNAi* testes (yellow dashed circle, Fig 4B-B'),
218 suggesting that NBs were disrupted after individualisation. Amongst the few remaining intact NBs,
219 more than 35% ($p = 0.0086$) were associated with severely deformed and thin baskets (Fig 4G-G'; pie
220 chart) with significantly lower volume (Fig 4I). Furthermore, the NB anisotropy estimate revealed a
221 lower trend (i.e., less ordered arrangement), although the difference was not statistically significant
222 (Fig 4J). The *DAAM RNAi* also caused a significant, but comparatively smaller reduction of NBs (Fig 4C-
223 D) than *dia RNAi*, with no alteration in the number of progressed ICs (Fig 4E, S5C). Similar to the *dia*
224 *RNAi*, nearly one-third of the baskets in the *DAAM RNAi* testes were thin and deformed (Fig 4H-H'; pie
225 chart) with marginally decreased volume (Fig 4I), suggesting that DAAM may also be involved in the
226 basket assembly. However, we did not observe a change in NB anisotropy (Fig 4J). Together, these
227 observations implicated both Dia and DAAM in the basket assembly.

228 Although *Frl* and *Form3 RNAi*s also severely reduced the number of intact NBs (Fig 4D; S5D,
229 G), the number of progressed ICs were also reduced significantly (Fig 4E; S5F, I). A few remaining NBs
230 that we found in these backgrounds appeared to have intact baskets (arrowheads, Fig S5E, H), but we
231 could not quantify their morphology, as the number of intact NBs was insufficient. Hence, we
232 concluded that the NBs were lost due to considerable disruption of an earlier differentiation process.
233 Lastly, the expression of *Fhos* and *Capu RNAi*s did not affect NB (Fig 4D; S5J, M) and IC (Fig 4E; S5 L, O)
234 counts. The basket morphologies were also similar to that of control (Fig S5 K, N, P). Also, Capu-GFP
235 did not localise at the basket (Fig S5Q-Q'). Therefore, the role of Fhos and Capu in basket assembly
236 was ruled out. Overall, on the basis of the genetic perturbations, the roles of formins in spermatid
237 maturation can be categorised as- affecting NBs but not ICs (Dia and DAAM), affecting both NBs and
238 ICs (Frl and Form 3), and affecting neither NBs nor ICs (Fhos and Capu).

239 Altogether, the genetic analysis suggested that the basket is exclusively formed through Dia
240 and DAAM. Consistent with this conjecture, we found a visible enrichment of Dia at the basket region

241 (arrowhead, Fig 4K-K'). Therefore, we concluded that the basket consists of contractile actin-
242 membrane scaffold formed by Rho1, Dia and DAAM activities.

243

244 **N-BAR protein, Amphiphysin, recruits Rho1 and activates the F-actin assembly at the basket domain**

245 Local tension and curvature of the membrane bilayer triggers F-actin assembly (Aspenstrom, 2014;
246 Yang and Saif, 2007). TEM sections revealed that extensively folded membrane surrounds the
247 spermatid heads (Fig 1E-G), and time-lapse observations after the laser ablation (Fig 2B) suggested
248 that the spermatid heads continuously press onto the HCC. Hence, mechanical tension along the HCC
249 plasma membrane could initiate the F-actin assembly forming the basket domain. Association of the
250 Clathrin-family of coat protein complex bends and stabilises the membrane curvature, and promotes
251 endocytosis (Hinrichsen et al., 2006). Also, the recruitment of BAR domain proteins onto negatively-
252 charged membrane buds stabilises the membrane curvature and activates the BAR domain proteins,
253 which sequester specific Rho-GTPases (Aspenstrom, 2014).

254 Expression of the GFP-tagged Clathrin-light-chain (*PpY>eGFP-Clc*, Fig 5A) and the BAR domain
255 protein Syndapin (*PpY>Synd-GFP,* Fig 5B-B') in the HCC marked the actin cap. The eGFP-Clc expression
256 surrounded the basket and the caplet domain (arrowhead and arrow, Fig 5A-A'), whereas Synd-GFP
257 co-localised with F-actin of the basket domain (arrows, Fig 5B-B'). Synd associates with the curved
258 membrane through the SH3 and the BAR-domain. The negatively charged Phosphatidylinositol 4, 5-
259 bisphosphate (PIP_2) is essential for Syndapin binding (Takeda et al., 2013). Overexpression of Synd-
260 SH3-eYFP (Fig S6A-A') marked the basket, whereas that of the Synd-R129E R130E-eYFP, carrying
261 mutations in the PIP_2 interacting residues of the BAR domain, failed to mark the basket (Fig S6B-B').
262 This result further indicated that the basket domain is rich in the negatively charged membrane,
263 particularly PIP_2. Therefore, to understand the role of membrane remodelling proteins in this process,
264 we performed a limited RNAi screen.

265 Clathrin consists of three heavy chains, each associated with a light chain. This triskelion
266 arrangement forms a cage-like lattice on the membrane (Kirchhausen et al., 2014). The clathrin heavy
267 chain (chc) and light chain (clc) RNAis did not alter the number of intact NBs in the TE (Fig 5E; S6E, G),
268 as well as the progressed ICs (Fig 5F; S6F, H). However, we noticed a small but significant decrease in
269 the number of mature baskets in the *chc RNAi* background (p=0.040, pie chart, Fig 5H). A similar
270 reduction was seen in *clc RNAi* testes, but the difference was not significant (pie chart, Fig 5I). Hence,
271 we concluded that though Clathrin may control the membrane flux in the basket region, it is unlikely
272 to have a central role in the basket assembly.

273 Amongst the BAR domain proteins, Synd (de Kreuk et al., 2011), Amphiphysin (Amph) (Yamada
274 et al., 2009), Cdc42 interacting protein (Cip4) (Fricke et al., 2009), Insulin Receptor Substrate 53 kDa
275 (IRSp53) (Goh et al., 2012) and Protein Interacting with C Kinase 1 (PICK1) (Rocca et al., 2008) are
276 implicated in actin polymerisation. Synd/PASCIN overexpression recruited Dia at the pseudocleavage
277 furrows of *Drosophila* embryos (Sherlekar and Rikhy, 2016); Cip4 binding antagonised Dia-induced
278 actin polymerisation (Yan et al., 2013); and IRSp53 binds to mDia during filopodia extension (Goh et
279 al., 2012). PICK1, on the other hand, is indicated to inhibit Arp2/3 (Rocca et al., 2008), and recruit F-
280 actin to the site of endocytosis through myosin (Madasu et al., 2015) in different contexts. Since Dia,
281 and potentially DAAM, are required for basket actin polymerisation, we tested the role of all these
282 BAR domain proteins in the basket assembly.

283 The *Synd*, *IRSp53* and *PICK1 RNAis* did not affect the number of intact NBs (Fig 5E; Fig S6I, N,
284 Q) and the IC progression (Fig 5F; Fig S6J, O, R). The basket morphology of *synd RNAi* testes was also
285 not significantly different from that of the control (Fig 5J-J'; pie chart). Similar results were obtained
286 due to the overexpression of the dominant-negative Synd-R129E R130E-eYFP (Fig S6C-D). Together,
287 these data ruled out a role of Synd/PASCIN, IRSp53 and PICK1 in the basket assembly.

288 In *amph RNAi* testes, there was a significant reduction in intact NBs (Fig 5E, K-K') with a large
289 proportion of them having relatively thin baskets or only actin sleeves (open arrow and pie chart, Fig
290 5K-K'). The IC progression was not affected (Fig 5F; Fig S6K). The defect was even more severe in the
291 *Cip4 RNAi* testes (Fig 5E, L-L'; Fig S6L). However, *Cip4 RNAi* also significantly reduced the number of
292 progressed ICs (Fig 5F; Fig S6M), suggesting that the loss of NB could be contributed by the disruption
293 of the upstream differentiation process.

294 Finally, in the *amph RNAi* background the Rho1 enrichment was eliminated from the thin
295 baskets (Fig 5N-N'). This observation is consistent with a recent study which suggested that Rvs 167,
296 the budding yeast homologue of Amph, is essential for the localisation of Rho1, in both a Rho GEF
297 dependent and independent manner during cytokinesis (Cundell and Price, 2014). Rho1 accumulates
298 at the cytokinetic furrow in a PIP_2-dependent manner (Yoshida et al., 2009). Furthermore, the
299 association of the BAR domain proteins stabilises phosphoinositide domains (Zhao et al., 2013). Hence,
300 we concluded that Amph and possibly the PIP_2 recruitment and stabilisation on the HCC membrane
301 surrounding the spermatid heads could recruit and activate Rho1, and promote the F-actin assembly,
302 as well as the basket morphogenesis.

303

304

305 **Non-muscle myosin-II maintains the F-actin structure and the integrity of the basket domain**

306 Time-lapse imaging revealed that the basket is a contractile structure (Fig 2A). In addition to Formins,
307 the GTP-bound Rho activates a serine/threonine kinase called Rho kinase (Rok/ROCK), which regulates
308 several cytoskeletal rearrangements by phosphorylating a large number of target proteins (Amano et
309 al., 2010). The Rok-GFP expression under the regulatory myosin-light-chain (*spaghetti-squash*)
310 promoter (*sqh::Rok-GFP*) highlighted Rok enrichment in the basket domain (arrowhead, Fig 6A-A').
311 One of the downstream targets of Rok is Spaghetti-squash (Sqh), the *Drosophila* orthologue of the
312 regulatory light chain (RLC) of the non-muscle-myosin-II (NM2) (www.flybase.org). NM2 exists in an
313 auto-inhibited folded confirmation. The phosphorylation at Thr 20 and/or Ser 21 of Sqh/RLC relieves
314 the heavy-chain (HC) (Zipper/ Zip in *Drosophila*) auto-inhibition and leads to oligomerisation of NM2
315 into bipolar filaments. Active NM2 oligomers crosslink F-actin into antiparallel bundles and generate
316 contractile force along the filament (Liu et al., 2017). NM2 drives morphogenetic movements, such as
317 dorsal closure, cytokinesis, and wound healing (Franke et al., 2010). We found that both Zip/HC and
318 Sqh/RLC localise at the basket in the *PpY>zip-GFP* (Fig 6B-B') and *sqh::sqh-GFP* (Fig 6C-C') backgrounds.
319 Also, phosphorylated Sqh/RLC (p-MLC) immunostaining exclusively labelled the basket domain (Fig
320 6D-D'). Thus, Rho1-dependent recruitment and activation of Rok are likely to promote the NM2
321 association with the basket.

322 In addition to the contractile behaviour, the laser ablation study suggested that basket
323 maintains the spermatid heads in a tight bundle (Fig 2B). Therefore, to understand whether an
324 actomyosin contraction is responsible for bundling the spermatid heads together, we perturbed the
325 functions of the Rok and NM2 complex in cyst cells. Expression of the *Rok RNAi* (Fig 6F-F') and the
326 dominant-negative *YFP-zip DN* transgene, lacking the actin-binding motor domain (Fig 6H-H') by *PpY-*
327 *Gal4* caused abnormal accumulation of disrupted spermatid bundles in the TE. These perturbations
328 also reduced the average NBs significantly (Fig 6I) without affecting the progressed ICs (Fig 6J; S7A, C).
329 Also, *sqh* knockdown (*Mlc RNAi*) severely affected both NB integrity and IC progression (Fig 6I-J; S7D-
330 E). As expected, the overexpression of the constitutive-active Rok catalytic domain (*Rok-CAT*)
331 selectively increased the NB accumulation (Fig 6I), without affecting ICs (Fig 6J; S7B). We also noted
332 that YFP-zip DN failed to localise at the basket domain (magenta, Fig 6N). Altogether, these results
333 indicated that NM2 localises to the basket directly through its motor domain, and the actomyosin
334 activity is essential for either the basket assembly or maintenance or both.

335 In the *Rok RNAi* testes, more than 45% of the NBs were associated with thin or deformed
336 baskets (pie chart, Fig 6L). The average volume of the basket domain was significantly reduced (Fig
337 6O). In contrast, more than 90% of the NBs in the *Rok-CAT* overexpression background had mature

338 baskets (pie chart, Fig 6M), with very similar volume to the control (Fig 6O). The similarity of the results
339 obtained from the Rho1CA (Fig 3) and Rok-CAT overexpression backgrounds suggest that upregulation
340 of the Rho-Rok pathway may stabilise the basket through the NM2 activation, which would reduce
341 the frequency of sperm release causing accumulation of NBs at the testicular base.

342 In both *Rok RNAi* and *YFP-zip DN* expressing testes, the proportion of mature baskets (Fig 6L,
343 N), the basket volume (Fig 6O), and the anisotropy of NB alignment (Fig 6P) were reduced. These
344 results suggested that the NM2 activity is essential for maintaining the F-actin level and the function
345 of the basket required for gathering the spermatid heads.

346 Regulation of the myosin activity is vital to prevent over-constriction of the actomyosin
347 cytoskeleton. The activity of myosin is maintained by reversible phosphorylation of Sqh/RLC through
348 the regulatory Myosin-binding-subunit (Mbs) protein (Mizuno et al., 2002) and the phosphatase -
349 Flapwing (Flw) (Kirchner et al., 2007). Mbs is inactivated through phosphorylation by Rok, which
350 inhibits the dephosphorylation of Sqh/RLC by Flw. Expression of the constitutively-active Mbs-N300,
351 lacking the N-terminal Rok phosphorylation site, reduced the number of intact NBs significantly
352 without affecting the IC progression (Fig 6I-J; S7F, G) which is consistent with the above conclusion.
353 However, contrary to our expectations, *Mbs* and *flw RNAis* had minimal effect on the NB accumulation
354 (Fig S8A), basket volume (Fig S8C) and basket morphology (Fig S8D, E). These results indicate that Mbs
355 and Flw are unlikely to regulate the NM2/RLC function at the basket. Also, the overexpression of
356 catalytically inactive Rok (Rok CAT-KG), the constitutively-active Sqh-EE and the dominant-negative
357 Sqh-AA, lacking both the phosphorylation sites, had no significant impact on NB count and basket
358 volume (Fig S8B and C). We reasoned that the level of Sqh-AA and Sqh-EE expression were inadequate
359 for interfering with the NM2 function at the basket.

360 Together, these results suggested that Rok-mediated activation of NM2 is essential for
361 maintaining the basket domain, and the actomyosin contractility keeps the NB together. Further, we
362 hypothesised that the NM2 activity would also be essential for maintaining the actin-membrane
363 scaffold in the basket region.

364

365 **Rok dynamically maintain the NM2 localisation and F-actin organisation in the basket domain**

366 To test these conjectures, we inhibited Rok activity by treating testis expressing either Sqh-GFP or Utr-
367 GFP with Rockout^{TM}, an ATP competitive inhibitor of Rok (Yarrow et al., 2005). Treatment with 200
368 µM Rockout for one hour significantly reduced the number of intact NBs (Fig 7A-C) and accumulated
369 disrupted spermatids within the TE (yellow dashed circle, Fig 7B). Although the DMSO treatment also

370 caused some abnormality, (arrowheads, Fig 7A-A'), the defects were severely enhanced upon Rockout
371 treatment (Fig 7B-B'). It also significantly disrupted the basket morphology (Fig 7D, E). Depth coding
372 indicated that NBs and associated actin caps remain within a compact volume inside the HCC in control
373 (Fig 7D'-D"). In contrast, most of the NBs appeared disrupted and spread over a large volume after the
374 Rockout treatment (Fig 7E', E''). The treatment also eliminated Sqh-GFP enrichment from the basket
375 (Fig 7D''', E''', and F)

376 The time-lapse imaging further suggested that the Rockout treatment dispersed the Sqh-GFP
377 enrichment around the NB in 30 minutes, and concomitantly the spermatid heads were dissociated
378 from each other (Fig 7H; Video S8), which was not seen upon the DMSO treatment (Fig 7G and I; Video
379 S7 and S9). The treatment also disrupted the basket marked by Utr-GFP in 20 minutes (arrowhead, Fig
380 7J; Video S10). Together these observations suggested that the Rok-dependent NM2 activation
381 localises the myosin motor onto the basket, which maintains the basket integrity and applies a
382 compacting force on the spermatid heads, to keep them in a parallel bundle. However, the Utr-GFP
383 did not disperse from the basket region upon the Rockout treatment. Hence, we concluded that Rok
384 and NM2 are not essential for the F-actin assembly at the basket.

385 Altogether, the above results suggest that mechanical tension on the somatic cyst cell
386 membrane and membrane curvature induced by the intruding spermatid heads could recruit and
387 activate specific BAR domain proteins, Amphiphysin and perhaps Cip4. The recruitment of BAR domain
388 proteins could further recruit and activate Rho1, triggering the F-actin assembly through the formins,
389 Dia and DAAM. Rho1 also recruits Rok, which activates NM2. Active NM2 crosslinks the actin filaments
390 at the membrane and exerts a lateral clamp-like contractile force gathering the spermatid heads into
391 a tight parallel bundle (Fig 8). The membrane-actomyosin scaffold also resists further intrusion by the
392 spermatid heads.

393

394 **Discussion:**

395 Membrane indentation is the first step of inducing mechanical damage to the plasma
396 membrane. Artificial deformation or indentation of tissue-cultured cells induces actin accumulation
397 at the site of indentation (Lou et al., 2019; Yang and Saif, 2007). Hence, above results provides the first
398 insight into the events initiated at the start of membrane puncturing completely *in vivo*. Also,
399 preliminary assessment suggested that the membrane-associated with the basket domain is rich in
400 $PI(4,5)P_2$, which is essential for the interaction with the BAR domain. Therefore, the spermatid head
401 intrusion is also likely to trigger local alteration of lipid metabolism at the HCC plasma membrane. The

402 mechanism that initiates the recruitment of specific BAR domain proteins to the membrane is unclear.
403 These results suggest that the basket domain would be a useful paradigm to investigate how the
404 membrane tension could alter membrane composition and promote specific recruitment of the BAR
405 domain proteins, particularly Amphiphysin and potentially Cip4, at the HCC plasma membrane.

406 The BAR domain proteins are shown to interact with the Cdc42 and Rac1 family of Rho-
407 GTPases and nucleate F-actin assembly through the WASP/WAVE NPFs (Fricke et al., 2009). A Cip4-
408 like protein, Cdc15/FBP17, is also shown to associate with Dia and DAAM, during the filopodia
409 assembly (Aspenstrom et al., 2006). The consequence of the interaction is still unclear. A separate
410 study further suggested that Cip4 antagonises Dia during the extension of membrane furrows in
411 *Drosophila* embryos (Yan et al., 2013). The genetic analysis suggests that the BAR domain proteins,
412 Amphiphysin and potentially Cip4, could initiate the F-actin assembly at the basket domain in the HCC,
413 exclusively through a Rho-Dia/DAAM-mediated process. The loss of Amph eliminated Rho1
414 recruitment at the basket domain, as well as F-actin assembly. Thus, the results provide an indication
415 of Amphiphysin-mediated F-actin assembly through Dia and DAAM *in vivo*. Further studies would be
416 required to confirm and understand the molecular basis of this interaction.

417 Above results, together with the earlier report (Dubey et al., 2016), also depict that the HCC
418 membrane curved around each invading spermatid head nucleates two distinct actin networks. The
419 dendritic F-actin associated with caplets form due to WASp-Arp2/3 recruitment and activation in
420 response to the inadvertent invasions, or spermatid head-butting, and is a somewhat transient event.
421 It exerts a counterforce along the direction of invasion to repel every intrusion (Dubey et al., 2016).
422 The F-actin at the basket, nucleated by the Rho1-Dia/DAAM pathway, downstream to Amphiphysin,
423 is relatively stable and applies a lateral contractile force due to actomyosin activity to bundle the
424 spermatid heads together, like a clamp. The genetic and pharmacological analyses show that these
425 two actin networks form independently on two mutually exclusive and radially segregated membrane
426 domains. They also form at different time scales. The caplets are transient and form within minutes
427 of the invasion. Hence, they indicate a cellular response to rapid change in membrane tension. The
428 baskets, on the other hand, grows slowly after individualisation and matures after coiling.

429 The context of the basket assembly provides a clue to the underlying trigger. The HCC and TCC
430 are equally extended during the individualisation stage with their respective plasma membranes
431 tightly stretched around the individual spermatids (Tokuyasu et al., 1972a). Post individualisation, the
432 cysts proceed for coiling, and the HCC contracts (Dubey et al., 2019; Tokuyasu et al., 1972b), which
433 could loosen and fold the excess membrane around spermatid heads triggering the recruitment of
434 Amphiphysin (Fig 8). Therefore, the basket connotes to a response generated due to a change of

435 membrane tension over time. We also find that the functions of Rho1 and Rac1 are mutually
436 antagonistic at the basket domain, and Rac1 may also have a negative influence on the caplet and
437 tubule dynamics. Thus, the paradigm provides an opportunity to tease out how cells sense,
438 discriminate and respond to stress dynamics in the membrane.

439 Together with the previous report (Dubey et al., 2016), it is clear that the basket and caplets
440 are composed by distinct F-actin networks. A similar juxtaposition of different F-actin was reported at
441 the immunological synapse in T-cells, and during wound healing in *Drosophila*. At the immunological
442 synapse, three types of actin networks - branched, linear and focal clusters - are arranged in a
443 concentric manner (Hammer et al., 2019). Each of these structures presumably helps in the clustering
444 of proteins such as T-cell receptors. As a result, disruption of the network leads to defects in receptor
445 clustering (Murugesan et al., 2016). During the wound closure in *Drosophila* embryo, F-actin networks
446 formed by the Rho1, Rac1, Cdc42 GTPases surround the wound site (Abreu-Blanco et al., 2014).
447 Although Annexin and prepatterning of RhoGEFs were implicated in the Rho GTPases recruitment
448 (Nakamura et al., 2017), how three distinct Rho-GTPase domains assemble on the membrane is still
449 uncertain. Also, since each of these actin networks is partially overlapping, and concentrically
450 arranged, any perturbation to any one of them, affects the others (Abreu-Blanco et al., 2014). Hence,
451 it is challenging to dissect specific roles and mechanisms of regulations.

452 In comparison, the actin domains on the HCC membrane encompassing the actin cap region
453 are mutually exclusive and well separated. Two distinct mechanical actions trigger them, and we now
454 demonstrated that one could independently perturb the basket and caplets. Therefore, it would be
455 interesting to study how two different F-actin nucleation mechanisms are established on the HCC
456 plasma membrane in real-time during sperm coiling and release in the future.

457 Finally, a majority of actomyosin structures are known to undergo constriction to achieve
458 complete closure, such as during cytokinesis, wound healing and dorsal closure. Specific actomyosin
459 arrangements also provide scaffolding or stabilising force. The actomyosin association with the
460 adherens junctions at the apical boundary of epithelia serves to stabilise the contact site and helps to
461 recruit the junctional components (Lecuit et al., 2011; Schwayer et al., 2016; Zenker et al., 2018). In
462 all these instances the actomyosin complex is organised in a ring-like form on a 2D-plane. Here, we
463 showed that a 3-D membrane-actomyosin assembly could generate lateral constricting force
464 orthogonal to the direction of intrusive force, to clasp the spermatid heads together. This finding
465 demonstrates a novel cell adhesion strategy, which is unprecedented. Further investigation is required
466 to identify the physical basis of such an assembly and its functioning.

467

468 **Materials and Methods:**

469 *Drosophila* stocks and culture

470 All *Drosophila* stocks and crosses were maintained in standard cornmeal media at 25 °C. Male progeny
471 of *UAS-RNAi* crosses was collected and kept at 28 °C for 4 days, to achieve optimum Gal4 expression.
472 All the stocks have been listed in Table S1. All experiments involving transgenic *Drosophila* lines were
473 approved by the Institute Bio-Safety Committee, DBT, Govt. of India.

474 Whole-mount immunostaining

475 Testes were dissected in 1x PBS and fixed for 30 mins in 4% paraformaldehyde (PFA), followed by 3
476 washes of 10 mins each, with 0.3% PTX (0.3% Triton X 100 in 1 x PBS). Immunostaining samples were
477 then incubated in blocking buffer (2 mg/ ml Bovine Serum Albumin (BSA) in 0.3% PTX) for 30 mins,
478 followed by overnight incubation in the primary antibody. Samples were then washed and incubated
479 with Alexa-conjugated secondary antibodies (Invitrogen) for 2 hours, followed by incubation in 0.001%
480 Hoechst 33342 (Sigma-Aldrich), and 10 µM FITC Phalloidin/ Atto 647 Phalloidin (Sigma-Aldrich) for 30
481 min. Samples were then washed and mounted with a drop of Vectorshield™ mounting medium on a
482 glass slide. The primary antibodies used were anti-Fas III (1:100, DSHB), anti-Rho 1 (1:100, DSHB), anti-
483 Dia (1:2500, courtesy Prof. S Wasserman, UCSD) and anti-pMLC (1:25, Cell Signalling Technologies).

484 STED (Stimulated Emission Depletion)

485 For STED imaging, *ProtB-dsRed* testes were processed as described above and stained with Atto647-
486 Phalloidin. The samples were mounted on glycerol, and #1.5 coverslips were used. Depletion for both
487 fluorophores was done using a 775 nm laser. Time gating of 0.6<tg>6.6 was applied. Images were
488 acquired in 2D STED mode.

489 *Ex vivo* time-lapse imaging of testis

490 Live imaging was performed as described previously (Dubey et al., 2016). Images were acquired using
491 either an Olympus FV3000 confocal laser scanning microscope with 60x, 1.42 NA oil objective, or
492 Olympus FV1000 confocal laser scanning microscope with 60x, 1.35 NA oil objective. Rockout
493 (Calbiochem) was used at a concentration of 200 µM. For FRAP, 1.4 μm^2 area in the basket was
494 bleached to 60% level using high intensity 488 nm laser for 2 seconds with 2 µs/pixel scan speed, and
495 the recovery profile was recorded at 5.5-second/frame rate. The data were analysed using ImageJ®
496 and Origin™.

497

498

499 Laser ablation

500 Laser ablation was performed using the Spectra-Physics Mai Tai Ti-Sapphire laser system on Zeiss 710
501 microscope. For ablation, 408.2 mW of 800 nm laser was focussed in 0.75 μm^2 (10x10 pixels) area for
502 five iterations with a pixel dwell time of 12.6 µs/pixel.

503 Image Analysis and Quantification

504 All images were analysed on ImageJ/Fiji® (ImageJ.net/Fiji). We used the Cell Counter™ Plugin
505 for the NB and IC estimation and the FibrilTool Plugin (Boudaoud et al., 2014), which measures the
506 orientation and anisotropy of fibrillary structures, to assess the parallel organisation of spermatid
507 heads in each NB. A value of 1 indicates purely anisotropic (perfectly ordered or parallel), and 0
508 indicates disordered assembly. For FRAP, the intensities in the SUM projection was calculated from
509 the FRAP ROI, as well as an arbitrary background ROI. The data was normalised and fitted to a single
510 exponential using the Levenberg-Marquardt iteration algorithm in Origin™ 2019, based on which
511 maximum recovery was calculated. The basket volume was estimated using Imaris™ (Bitplane AG). A
512 volume filter of 100 voxels was applied, to eliminate stray F-actin puncta in the given ROI. For basket
513 morphology analysis, there was a very small proportion of NBs for which we could not determine the
514 basket morphology, due to technical reasons, such as if the NB was oriented perpendicular to the
515 plane of imaging. These were categorized as 'undetermined'.

516 Statistical analyses (One-way ANOVA, Mann-Whitney Test) were carried out using Origin™ 2019.
517 Fisher's exact test was performed using the Graphpad online calculator. For box and dot plots, 'n'
518 values are indicated by the number of dots. For Fisher's exact test, 'n' values are indicated near the
519 pie chart or on the stacked bar graph.

520

521 Transmission Electron Microscopy

522 TEM samples were prepared as per the previous description (Dubey et al., 2019).

523

524 **Acknowledgements:**

525 We thank Richa Ricky, Benny Shilo, Steven Wasserman, Andrea Brand, John Belote, Vimlesh Kumar,
526 Thomas Lecuit, and Eyal Schejter for generous sharing of reagents. We acknowledge the BDSC, VDRC,
527 DSHB, IISER Pune fly facility and NCBS Fly Facility, India for providing fly stocks and antibodies. We also
528 thank Lalit Borde for help with TEM, and Hina Mohammed for assistance with the Synd mutant
529 experiment. We are grateful to Prof. Shilo for his continuous guidance and support.

530 **Authors' contributions:**

531 TK and PD performed the experiments. TK and KR wrote the manuscript. SS provided the TEM data.

532 **Funding**:

533 TK, PD and KR were supported by the intramural grant of Dept. of Atomic Energy (DAE), Government
534 of India, to TIFR. The study was supported by the DAE, TIFR grant 12-R&D-TFR-5.10-100; Department
535 of Atomic Energy, Government of India.

536 **Disclosure statement:**

537 The authors have no competing interests.

538

539 **References:**

540 Abagnale, G., Steger, M., Nguyen, V.H., Hersch, N., Sechi, A., Joussen, S., Denecke, B., Merkel, R.,
541 Hoffmann, B., Dreser, A.*, et al.* (2015). Surface topography enhances differentiation of mesenchymal
542 stem cells towards osteogenic and adipogenic lineages. Biomaterials *61*, 316-326.
543 Abreu-Blanco, M.T., Verboon, J.M., and Parkhurst, S.M. (2014). Coordination of Rho family GTPase
544 activities to orchestrate cytoskeleton responses during cell wound repair. Curr Biol *24*, 144-155.
545 Amano, M., Nakayama, M., and Kaibuchi, K. (2010). Rho-kinase/ROCK: A key regulator of the
546 cytoskeleton and cell polarity. Cytoskeleton (Hoboken) *67*, 545-554.
547 Aspenstrom, P. (2014). BAR domain proteins regulate Rho GTPase signaling. Small GTPases *5*, 7.
548 Aspenstrom, P., Richnau, N., and Johansson, A.S. (2006). The diaphanous-related formin DAAM1
549 collaborates with the Rho GTPases RhoA and Cdc42, CIP4 and Src in regulating cell morphogenesis
550 and actin dynamics. Exp Cell Res *312*, 2180-2194.
551 Boudaoud, A., Burian, A., Borowska-Wykret, D., Uyttewaal, M., Wrzalik, R., Kwiatkowska, D., and
552 Hamant, O. (2014). FibrilTool, an ImageJ plug-in to quantify fibrillar structures in raw microscopy
553 images. Nat Protoc *9*, 457-463.
554 Breitsprecher, D., and Goode, B.L. (2013). Formins at a glance. J Cell Sci *126*, 1-7.
555 Cundell, M.J., and Price, C. (2014). The budding yeast amphiphysin complex is required for
556 contractile actin ring (CAR) assembly and post-contraction GEF-independent accumulation of Rho1-
557 GTP. PLoS One *9*, e97663.
558 de Kreuk, B.J., Nethe, M., Fernandez-Borja, M., Anthony, E.C., Hensbergen, P.J., Deelder, A.M.,
559 Plomann, M., and Hordijk, P.L. (2011). The F-BAR domain protein PACSIN2 associates with Rac1 and
560 regulates cell spreading and migration. J Cell Sci *124*, 2375-2388.
561 Desai, B.S., Shirolikar, S., and Ray, K. (2009). F-actin-based extensions of the head cyst cell adhere to
562 the maturing spermatids to maintain them in a tight bundle and prevent their premature release in
563 Drosophila testis. BMC Biol *7*, 19.
564 Dubey, P., Kapoor, T., Gupta, S., Shirolikar, S., and Ray, K. (2019). Atypical septate junctions maintain
565 the somatic enclosure around maturing spermatids and prevent premature sperm release in
566 Drosophila testis. Biol Open *8*.
567 Dubey, P., Shirolikar, S., and Ray, K. (2016). Localised, Reactive F-Actin Dynamics Prevents Abnormal
568 Somatic Cell Penetration by Mature Spermatids. Dev Cell *38*, 507-521.
569 Franke, J.D., Montague, R.A., and Kiehart, D.P. (2010). Nonmuscle myosin II is required for cell
570 proliferation, cell sheet adhesion and wing hair morphology during wing morphogenesis. Dev Biol
571 *345*, 117-132.

572 Fricke, R., Gohl, C., Dharmalingam, E., Grevelhorster, A., Zahedi, B., Harden, N., Kessels, M.,
573 Qualmann, B., and Bogdan, S. (2009). Drosophila Cip4/Toca-1 integrates membrane trafficking and
574 actin dynamics through WASP and SCAR/WAVE. Curr Biol *19*, 1429-1437.
575 Ghosh-Roy, A., Desai, B.S., and Ray, K. (2005). Dynein light chain 1 regulates dynamin-mediated F-
576 actin assembly during sperm individualisation in Drosophila. Mol Biol Cell *16*, 3107-3116.
577 Goh, W.I., Lim, K.B., Sudhaharan, T., Sem, K.P., Bu, W., Chou, A.M., and Ahmed, S. (2012). mDia1 and
578 WAVE2 proteins interact directly with IRSp53 in filopodia and are involved in filopodium formation. J
579 Biol Chem *287*, 4702-4714.
580 Guttman, J.A., Takai, Y., and Vogl, A.W. (2004). Evidence that tubulobulbar complexes in the
581 seminiferous epithelium are involved with internalisation of adhesion junctions. Biol Reprod *71*, 548-
582 559.
583 Hammer, J.A., Wang, J.C., Saeed, M., and Pedrosa, A.T. (2019). Origin, Organization, Dynamics, and
584 Function of Actin and Actomyosin Networks at the T Cell Immunological Synapse. Annual Review of
585 Immunology *37*, 201-224.
586 Hinrichsen, L., Meyerholz, A., Groos, S., and Ungewickell, E.J. (2006). Bending a membrane: how
587 clathrin affects budding. Proc Natl Acad Sci U S A *103*, 8715-8720.
588 Kirchhausen, T., Owen, D., and Harrison, S.C. (2014). Molecular structure, function, and dynamics of
589 clathrin-mediated membrane traffic. Cold Spring Harb Perspect Biol *6*, a016725.
590 Kirchner, J., Gross, S., Bennett, D., and Alphey, L. (2007). The nonmuscle myosin phosphatase
591 PP1beta (flapwing) negatively regulates Jun N-terminal kinase in wing imaginal discs of Drosophila.
592 Genetics *175*, 1741-1749.
593 Kuhn, S., and Geyer, M. (2014). Formins as effector proteins of Rho GTPases. Small GTPases *5*,
594 e29513.
595 Lecuit, T., Lenne, P.F., and Munro, E. (2011). Force generation, transmission, and integration during
596 cell and tissue morphogenesis. Annu Rev Cell Dev Biol *27*, 157-184.
597 Liu, X., Billington, N., Shu, S., Yu, S.H., Piszczek, G., Sellers, J.R., and Korn, E.D. (2017). Effect of ATP
598 and regulatory light-chain phosphorylation on the polymerisation of mammalian nonmuscle myosin
599 II. Proc Natl Acad Sci U S A *114*, E6516-E6525.
600 Lou, H.Y., Zhao, W., Li, X., Duan, L., Powers, A., Akamatsu, M., Santoro, F., McGuire, A.F., Cui, Y.,
601 Drubin, D.G.*, et al.* (2019). Membrane curvature underlies actin reorganisation in response to
602 nanoscale surface topography. Proc Natl Acad Sci U S A *116*, 23143-23151.
603 Madasu, Y., Yang, C., Boczkowska, M., Bethoney, K.A., Zwolak, A., Rebowski, G., Svitkina, T., and
604 Dominguez, R. (2015). PICK1 is implicated in organelle motility in an Arp2/3 complex-independent
605 manner. Mol Biol Cell *26*, 1308-1322.
606 Mizuno, T., Tsutsui, K., and Nishida, Y. (2002). Drosophila myosin phosphatase and its role in dorsal
607 closure. Development *129*, 1215-1223.
608 Murugesan, S., Hong, J., Yi, J., Li, D., Beach, J.R., Shao, L., Meinhardt, J., Madison, G., Wu, X., Betzig,
609 E.*, et al.* (2016). Formin-generated actomyosin arcs propel T cell receptor microcluster movement at
610 the immune synapse. Journal of Cell Biology *215*, 383-399.
611 Nakamura, M., Verboon, J.M., and Parkhurst, S.M. (2017). Prepatterning by RhoGEFs governs Rho
612 GTPase spatiotemporal dynamics during wound repair. J Cell Biol *216*, 3959-3969.
613 Noguchi, T., and Miller, K.G. (2003). A role for actin dynamics in individualisation during
614 spermatogenesis in Drosophila melanogaster. Development *130*, 1805-1816.
615 Pontes, B., Ayala, Y., Fonseca, A.C., Romao, L.F., Amaral, R.F., Salgado, L.T., Lima, F.R., Farina, M.,
616 Viana, N.B., Moura-Neto, V.*, et al.* (2013). Membrane elastic properties and cell function. PLoS One
617 *8*, e67708.
618 Rocca, D.L., Martin, S., Jenkins, E.L., and Hanley, J.G. (2008). Inhibition of Arp2/3-mediated actin
619 polymerisation by PICK1 regulates neuronal morphology and AMPA receptor endocytosis. Nat Cell
620 Biol *10*, 259-271.
621 Schwayer, C., Sikora, M., Slovakova, J., Kardos, R., and Heisenberg, C.P. (2016). Actin Rings of Power.
622 Dev Cell *37*, 493-506.

623 Sherlekar, A., and Rikhy, R. (2016). Syndapin promotes pseudocleavage furrow formation by actin
624 organisation in the syncytial Drosophila embryo. Mol Biol Cell *27*, 2064-2079.
625 Takeda, T., Robinson, I.M., Savoian, M.M., Griffiths, J.R., Whetton, A.D., McMahon, H.T., and Glover,
626 D.M. (2013). Drosophila F-BAR protein Syndapin contributes to coupling the plasma membrane and
627 contractile ring in cytokinesis. Open Biol *3*, 130081.
628 Tokuyasu, K.T., Peacock, W.J., and Hardy, R.W. (1972a). Dynamics of spermiogenesis in Drosophila
629 melanogaster. I. Individualisation process. Z Zellforsch Mikrosk Anat *124*, 479-506.
630 Tokuyasu, K.T., Peacock, W.J., and Hardy, R.W. (1972b). Dynamics of spermiogenesis in Drosophila
631 melanogaster. II. Coiling process. Z Zellforsch Mikrosk Anat *127*, 492-525.
632 Viswanathan, P., Ondeck, M.G., Chirasatitsin, S., Ngamkham, K., Reilly, G.C., Engler, A.J., and
633 Battaglia, G. (2015). 3D surface topology guides stem cell adhesion and differentiation. Biomaterials
634 *52*, 140-147.
635 Wiegand, T., Fratini, M., Frey, F., Yserentant, K., Liu, Y., Weber, E., Galior, K., Ohmes, J., Braun, F.,
636 Herten, D.-P.*, et al.* (2020). Forces during cellular uptake of viruses and nanoparticles at the ventral
637 side. Nature Communications *11*, 32.
638 Yamada, H., Padilla-Parra, S., Park, S.J., Itoh, T., Chaineau, M., Monaldi, I., Cremona, O., Benfenati, F.,
639 De Camilli, P., Coppey-Moisan, M.*, et al.* (2009). Dynamic interaction of amphiphysin with N-WASP
640 regulates actin assembly. J Biol Chem *284*, 34244-34256.
641 Yan, S., Lv, Z., Winterhoff, M., Wenzl, C., Zobel, T., Faix, J., Bogdan, S., and Grosshans, J. (2013). The
642 F-BAR protein Cip4/Toca-1 antagonises the formin Diaphanous in membrane stabilisation and
643 compartmentalisation. J Cell Sci *126*, 1796-1805.
644 Yang, S., and Saif, M.T. (2007). Force response and actin remodeling (agglomeration) in fibroblasts
645 due to lateral indentation. Acta Biomater *3*, 77-87.
646 Yarrow, J.C., Totsukawa, G., Charras, G.T., and Mitchison, T.J. (2005). Screening for cell migration
647 inhibitors via automated microscopy reveals a Rho-kinase inhibitor. Chem Biol *12*, 385-395.
648 Yoshida, S., Bartolini, S., and Pellman, D. (2009). Mechanisms for concentrating Rho1 during
649 cytokinesis. Genes Dev *23*, 810-823.
650 Zenker, J., White, M.D., Gasnier, M., Alvarez, Y.D., Lim, H.Y.G., Bissiere, S., Biro, M., and Plachta, N.
651 (2018). Expanding Actin Rings Zipper the Mouse Embryo for Blastocyst Formation. Cell *173*, 776-791
652 e717.
653 Zhao, H., Michelot, A., Koskela, E.V., Tkach, V., Stamou, D., Drubin, D.G., and Lappalainen, P. (2013).
654 Membrane-sculpting BAR domains generate stable lipid microdomains. Cell Rep *4*, 1213-1223.
655 Zhao, W., Hanson, L., Lou, H.Y., Akamatsu, M., Chowdary, P.D., Santoro, F., Marks, J.R., Grassart, A.,
656 Drubin, D.G., Cui, Y.*, et al.* (2017). Nanoscale manipulation of membrane curvature for probing
657 endocytosis in live cells. Nat Nanotechnol *12*, 750-756.

658

Main Figures and legends:

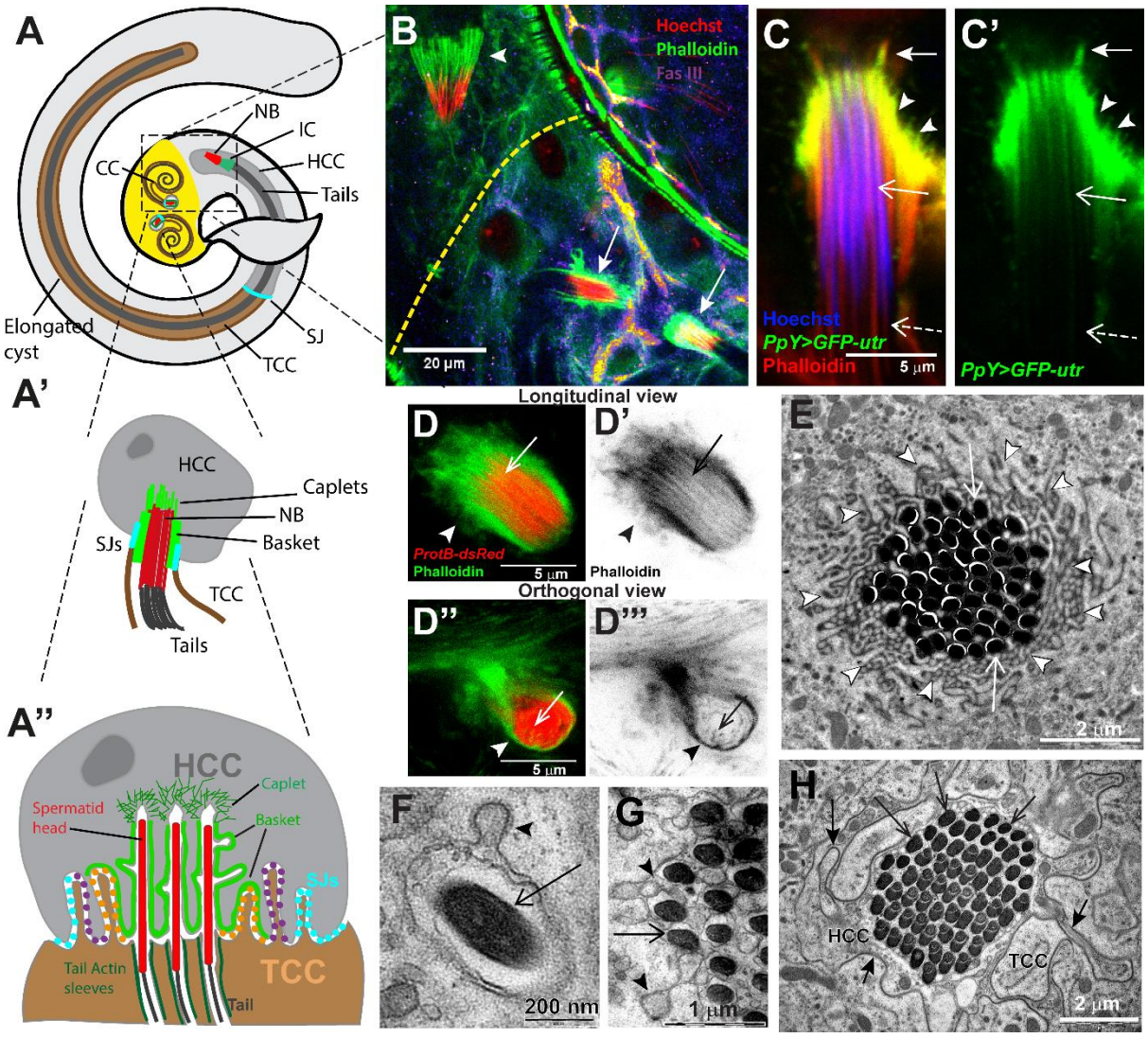

Figure 1- Network of tubular, actin-rich membrane covers individual spermatid heads within a cyst during the final stages of sperm maturation in *Drosophila* testis.

A-A'') Schematic of *Drosophila* testis. Sixty-four spermatids synchronously develop within the cyst enclosure. After individualisation, the elongated spermatid tails (dark grey) coil up inside the cyst and move to the TE region (yellow zone) at the base of the testis. The nuclei bundles or NBs (red) of coiled spermatids are covered by an actin cap (green), consisting of basket and caplet domains. **A'** and **A"** depicts the expanded views of the arrangement inside the HCC. As depicted in **A",** each spermatid head is enclosed with an actin-rich membrane sleeve. The HCC-TCC interface is highly folded, and marked by the SJs.

671 **B)** Confocal image of a wild-type testis, stained with Hoechst dye (red), marking the spermatid heads,
672 and Phalloidin (green) marking F-actin. Actin-caps form around the spermatid head bundles (NB, red)
673 (arrows) once the cyst is inside the TE region. The yellow dashed line marks the boundary of TE region
674 marked by the Fas-III immunostaining (Fire LUT). Arrowhead indicates the spermatid head bundle of
675 an early individualising cyst, with associated IC at the caudal end of the NB outside the TE region.

676 **C-C')** *PpY>GFP-utr* (green) expression in cyst cells, stained with Hoechst (blue) and Phalloidin (red).
677 The caplets (arrow) and the basket domains (arrowheads), as well as a part the actin sleeves (open
678 arrows), are marked by the GFP-Utr.

679 **D-D''')** STED microscopy images of NB (red) and associated actin cap (green) in *ProtB-dsRed* expressing
680 testis, stained with Phalloidin. The longitudinal view (D-D') shows that the actin structure is present in
681 between the packing of individual sperm heads (arrows). Orthogonal section (D''-D''') through the NB
682 also depicts the presence of actin in the region between individual sperm heads (arrows). Arrowheads
683 mark the basket actin surrounding the entire bundle.

684 **E-H)** TEM images of transverse sections of NBs from wild-type testes depict spermatid heads (open
685 arrows, E) surrounded by extensively folded and tubular membrane (arrowheads, E) near the tips of
686 the spermatid heads, which are buried relatively deeper inside the HCC. Such tubular membrane was
687 not visible at the level of the HCC-TCC junction (arrows, F). High magnification images of individual
688 spermatid heads inside the HCC (G) shows two layers of plasma membrane surrounding each
689 spermatid head. The outer layer, likely to be contributed by the HCC, have tubulobulbar extensions
690 (arrowheads, H).

691

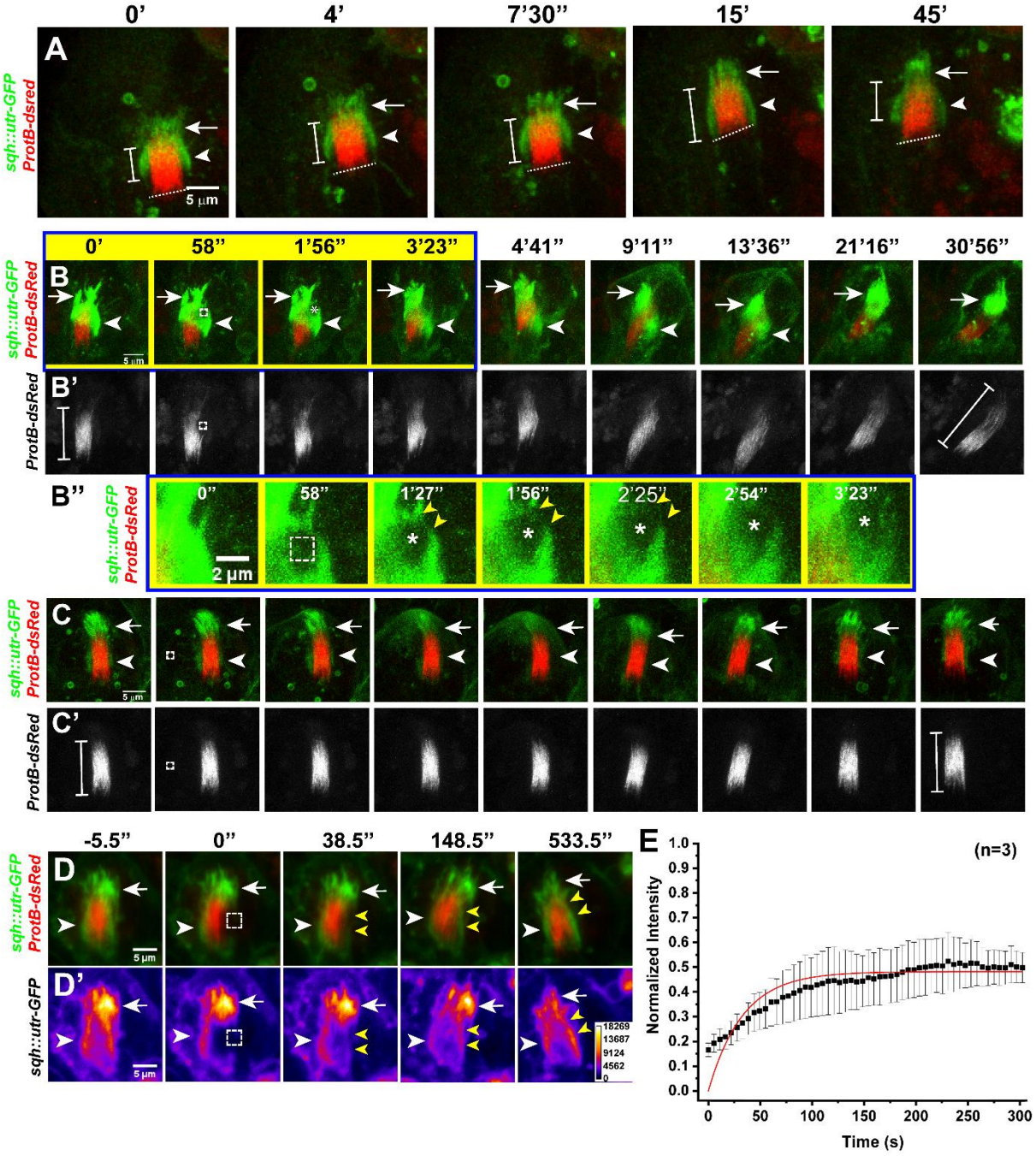

692

693

694 **Figure 2- Basket domain maintains the spermatid heads in a bundle.**

695 **A)** Time-lapse images of *sqh::utr-GFP; ProtB-dsRed* expressing testis, depicting the actin cap (green)
696 around the NB (red). Arrow indicates the caplet; the arrowheads indicate the basket domain, and the
697 dashed line denotes the caudal end of the NB. Note that the length of the basket, indicated by the
698 scale bar, oscillates along the long axis.

699 **B-C)** Time-lapse images after part ablation (dashed outline) of the basket domain (B-B''), and a control
700 spot in the HCC cytoplasm (C-C'), of *sqh::utr-GFP; ProtB-dsRed* testes, using 800 nm laser. Arrows mark

701 the caplets; the arrowheads mark basket and asterisks mark the centre of the ablated ROI. Closed lines
702 indicate the length of the NB, before ablations, and at 30'56". (B") High magnification images of 0-
703 3'23" frames of B, showing the expanding edges of the ablated region (yellow arrowheads).

704 **D)** Fluorescence recovery after photobleaching (FRAP) of *sqh::utr-GFP* in the basket domain. The
705 intensity profile is depicted in a false colour heat map (FIRE, D'). The dashed outline marks the
706 photobleached ROI; yellow arrowheads mark the photobleached zone during recovery; the
707 arrowheads mark the basket domain, and the arrows mark the caplets.

708 **E)** The FRAP recovery profile (mean ± S.D.) fitted with the Levenberg-Marquardt iteration algorithm.

709

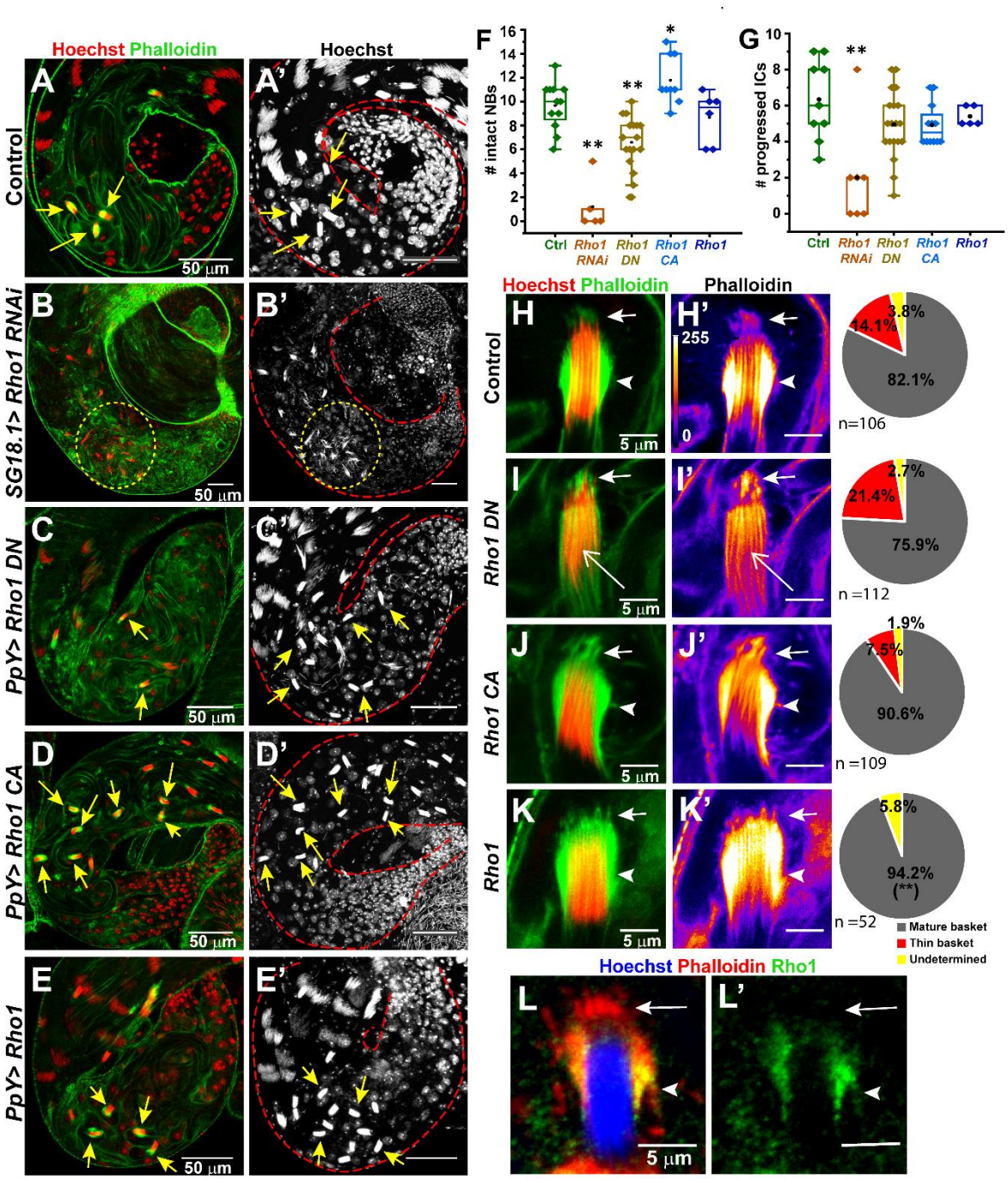

Figure 3- Rho 1 perturbation in the cyst cells affects the stability of the basket domain and NB.

A-E) Confocal sections of testes base from the Control (A-A'), *SG18.1>Rho1* RNAi (B-B'), *PpY>Rho1N19DN* (C-C'), *PpY>Rho1V14CA* (D-D') and *PpY>Rho1* (E-E') backgrounds, stained with the Hoechst (red/ white) and Phalloidin (green). Arrows indicate intact NBs associated with baskets. A'-E' represent maximum intensity projections of Hoechst channel, depicting all the NBs in the testes.

F-G) Box plots depict the number of intact NBs (F) and the progressed ICs (G) upon Rho 1 perturbations in the cyst cells. The pairwise significance with respect to the control value was estimated using One-

718 way Anova® and Mann-Whitney U tests, respectively, and the p-values- * <0.05, ** <0.01, *** < 0.001
719 are indicated on each box.

720 **H-K**) High magnification images of an NB associated with the actin cap from the control (G-G'), *Rho*
721 *1DN* (I-I'), *Rho 1CA* (J-J'), and *Rho 1* (J-J') expressing testes, stained with Hoechst (red) and Phalloidin
722 (green/ FIRE). Arrows, arrowheads and open arrows indicate caplets, basket, and actin sleeves,
723 respectively. Pie charts indicate relative proportions of different basket morphologies classified as
724 mature (as shown in Fig S1F), thin (as shown in S1G), and undetermined. The pairwise significance
725 with respect to the control value was estimated using Fisher's Exact test, and the p-values- * <0.05,
726 ** <0.01, *** < 0.001 are indicated on the pie chart.

727 **L-L)** NB and the associated basket domain stained with anti-Rho1 (green), Hoechst (blue), and
728 Phalloidin (red). Note that Rho1 is enriched at the basket domain (arrowhead), and not in the caplet
729 (arrow).

730

731

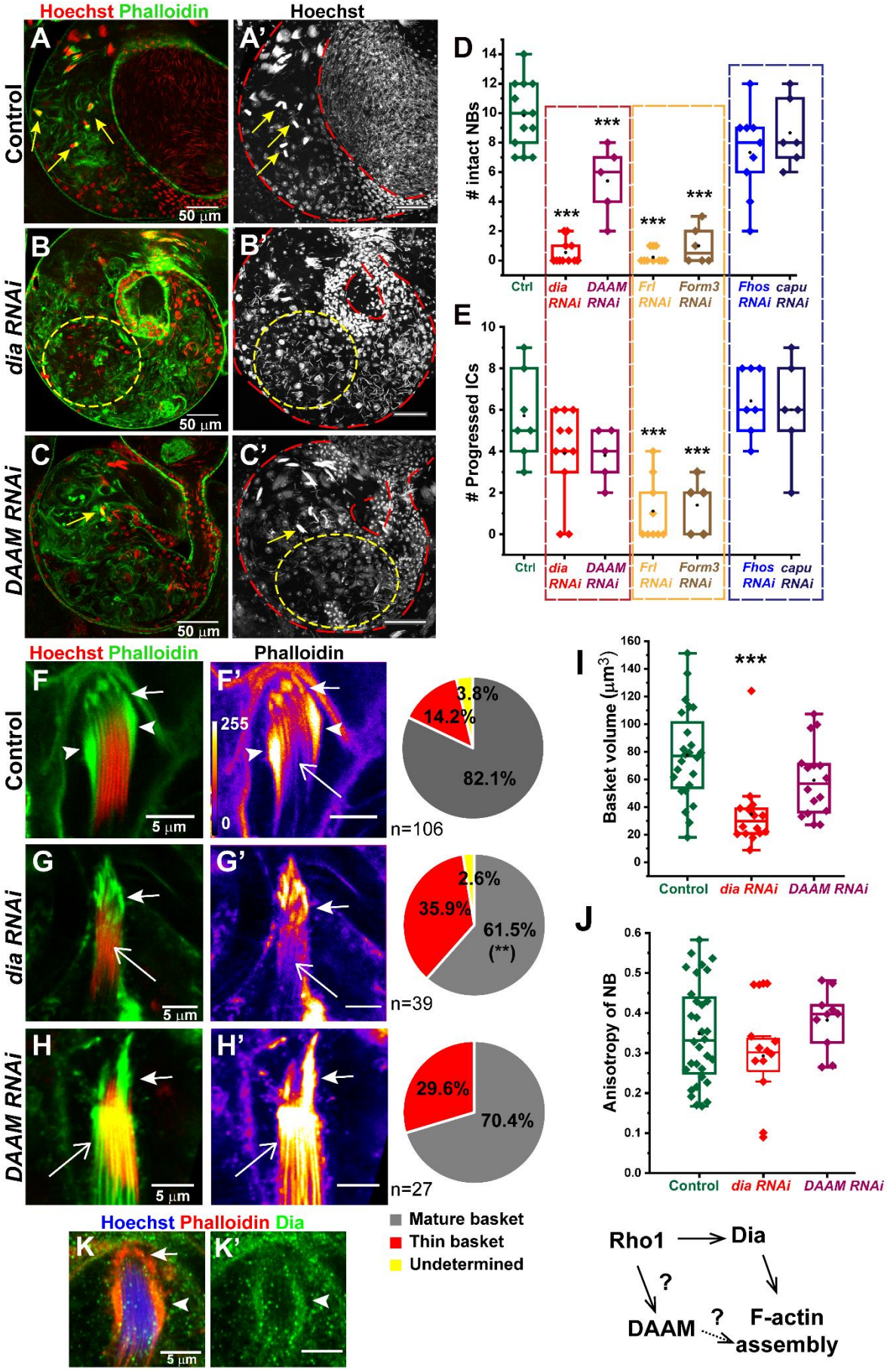
Hoechst Phalloidin
Hoechst
Control
dia RNAi
DAAM RNAi
A
A'
B
B'
C
C'
50 µm
D
intact NBs
Ctrl
dia RNAi
DAAM RNAi
Frl RNAi
Form3 RNAi
Fhos RNAi
capu RNAi
***
E
Progressed ICs
Hoechst Phalloidin
Phalloidin
F
F'
G
G'
H
H'
255
0
5 µm
3.8%
14.2%
82.1%
n=106
2.6%
35.9%
61.5%
(**)
n=39
29.6%
70.4%
n=27
Mature basket
Thin basket
Undetermined
I
Basket volume (µm³)
Control
dia RNAi
DAAM RNAi
J
Anisotropy of NB
Hoechst Phalloidin Dia
K
K'
Rho1
Dia
?
DAAM
F-actin assembly

732

733 **Figure 4- F-actin, nucleated by the formin, Diaphanous and DAAM, constitutes the basket domain.**

734 **A-C)** TE regions of *PpY>GFP* (Control, A-A'), *PpY> dia RNAi* (B-B') and *PpY> DAAM RNAi* (C-C') testes
735 stained with Hoechst (red/ white) and Phalloidin (green). A'-C' represent maximum intensity
736 projections, depicting all the NBs in the TE region.

737 **D-E)** Box plots depict the number of intact NBs (D) and the progressed ICs (E) on perturbation of six
738 different formins in the cyst cells. The pairwise significance with respect to the control value was
739 estimated using Mann-Whitney U tests, and the p-values- * <0.05, ** <0.01, *** < 0.001 are indicated
740 on each box.

741 **F-H)** High magnification images of NBs stained with Hoechst (red) and Phalloidin (green/FIRE), from
742 the control (F-F'), *dia* (G-G') and *DAAM* (H-H') *RNAi* testes. Pie charts indicate relative proportions of
743 different basket phenotypes. Arrows, arrowheads and open arrows indicate caplets, basket, and actin
744 sleeves, respectively. Significance was calculated using Fisher's exact test, and the p values - * <0.05,
745 ** <0.01, *** < 0.001 are indicated on the pie charts.

746 **I-J)** Box and dot plots depict the volume of the basket domain (I) and the organisation (Anisotropy) of
747 spermatid head alignment in the NBs (J) in Control, *dia* and *DAAM* RNAi backgrounds. The pairwise
748 significance of difference with respect to the control values was estimated using Mann-Whitney U
749 tests and One-way Anova®, respectively, and the p-values- * <0.05, ** <0.01, *** < 0.001 are indicated
750 on each box.

751 **K)** NB and the associated basket domain stained with anti-Dia (green), Hoechst dye (blue), and
752 Phalloidin (red). Note that Diaphanous is enriched at the basket domain (arrowheads), and not in the
753 caplet (arrow).

754

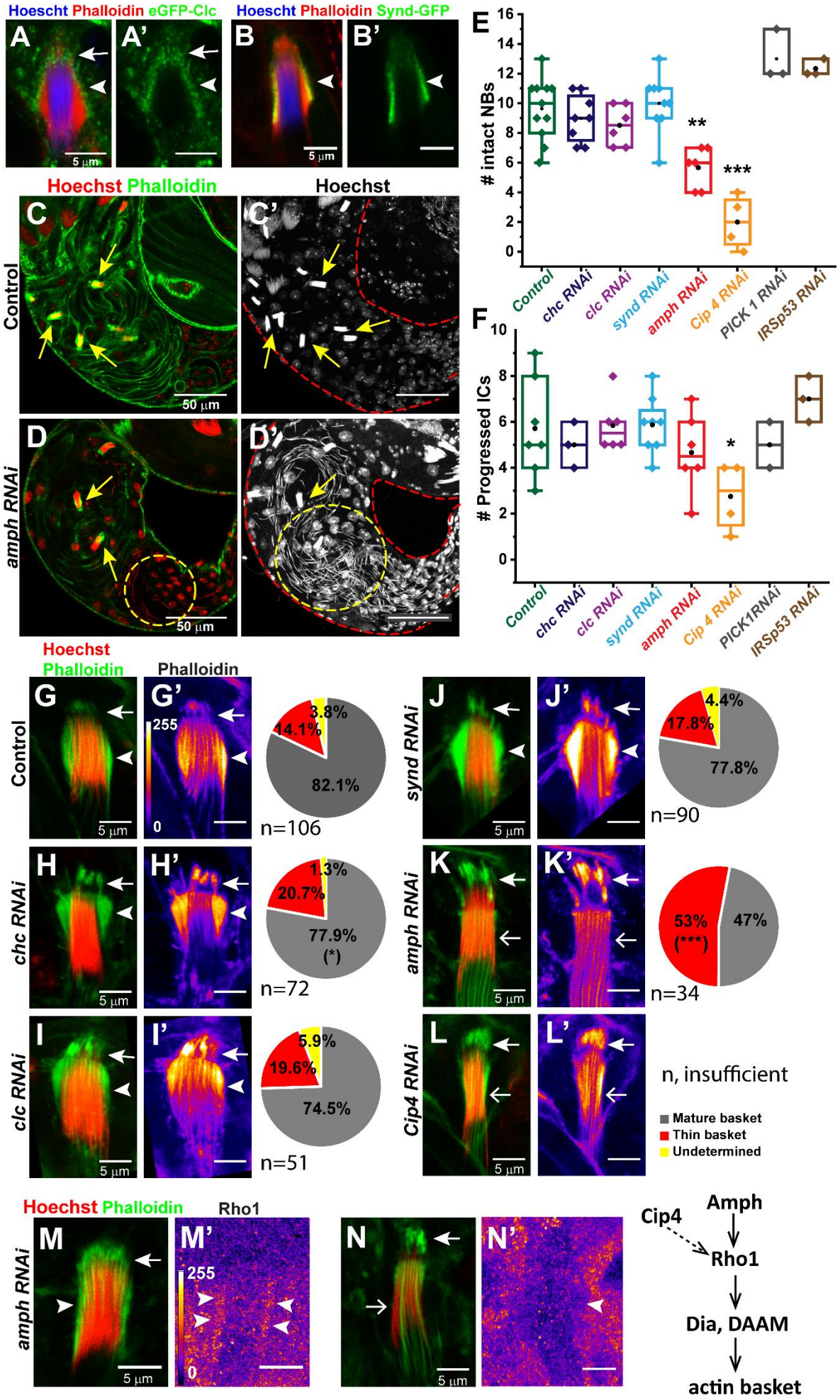
Hoescht Phalloidin eGFP-Clc
Hoescht Phalloidin Synd-GFP
A
A'
B
B'
5 µm
Hoechst Phalloidin
Hoechst
C
C'
D
D'
Control
amph RNAi
50 µm
E
intact NBs
**
***
Control
chc RNAi
clc RNAi
synd RNAi
amph RNAi
Cip 4 RNAi
PICK 1 RNAi
IRSp53 RNAi
F
Progressed ICs
*
PICK1RNAi
Hoechst
Phalloidin
Phalloidin
G
G'
255
0
3.8%
14.1%
82.1%
n=106
J
J'
synd RNAi
4.4%
17.8%
77.8%
n=90
H
H'
chc RNAi
1.3%
20.7%
77.9%
(*)
n=72
K
K'
amph RNAi
53%
(***)
47%
n=34
I
I'
clc RNAi
5.9%
19.6%
74.5%
n=51
L
L'
Cip4 RNAi
n, insufficient
Mature basket
Thin basket
Undetermined
Hoechst Phalloidin
Rho1
M
M'
N
N'
Cip4
Amph
Rho1
Dia, DAAM
actin basket

756 **Figure 5- The BAR domain proteins, Amphiphysin and Cip4, are required to assemble the basket**
757 **domain.**

758 **A-B)** Clathrin-Light-Chain (*PpY>e-GFP clc)* (A-A'), and Syndapin (*PpY> synd-GFP*) (B-B') localisations
759 around and in the basket domain (arrowheads).

760 **C-D)** Confocal images of TE of Control (C-C') and *amph RNAi* (D-D') testes, stained with Hoechst (red/
761 white) and Phalloidin (green). C', D' represent maximum intensity projections of the Hoechst channel,
762 depicting all the NBs in the testes. Yellow arrows mark intact testes, and yellow dashed circle marks
763 disrupted NBs.

764 **E-F)** Box and dot plots depicting the number of intact NBs (E) and the progressed ICs (F) in the testes
765 expressing different RNAi constructs in the cyst cells. The pairwise significance of difference with
766 respect to the control value was estimated using Mann-Whitney U tests, and the p-values- * <0.05, **
767 <0.01, *** < 0.001 are indicated on each box.

768 **G-L)** The morphology of the caplet (arrows) and the basket (arrowheads) domains in different RNAi
769 backgrounds, stained with the Hoechst dye (red) and Phalloidin (green/ FIRE). F-actin levels are
770 depicted in a false colour heat map (FIRE) in the right panels, and the associated pie charts depict the
771 penetrance of the phenotypes in these backgrounds. Open arrows indicate actin sleeves around the
772 spermatid tails.

773 **M-N)** Rho1 localisation (FIRE, M', N') in the *amph RNAi* background, stained with the Hoechst dye (red)
774 and Phalloidin (green). Arrows indicate the caplets, arrowheads indicate the basket, and the open
775 arrow indicates the actin sleeve, respectively.

776

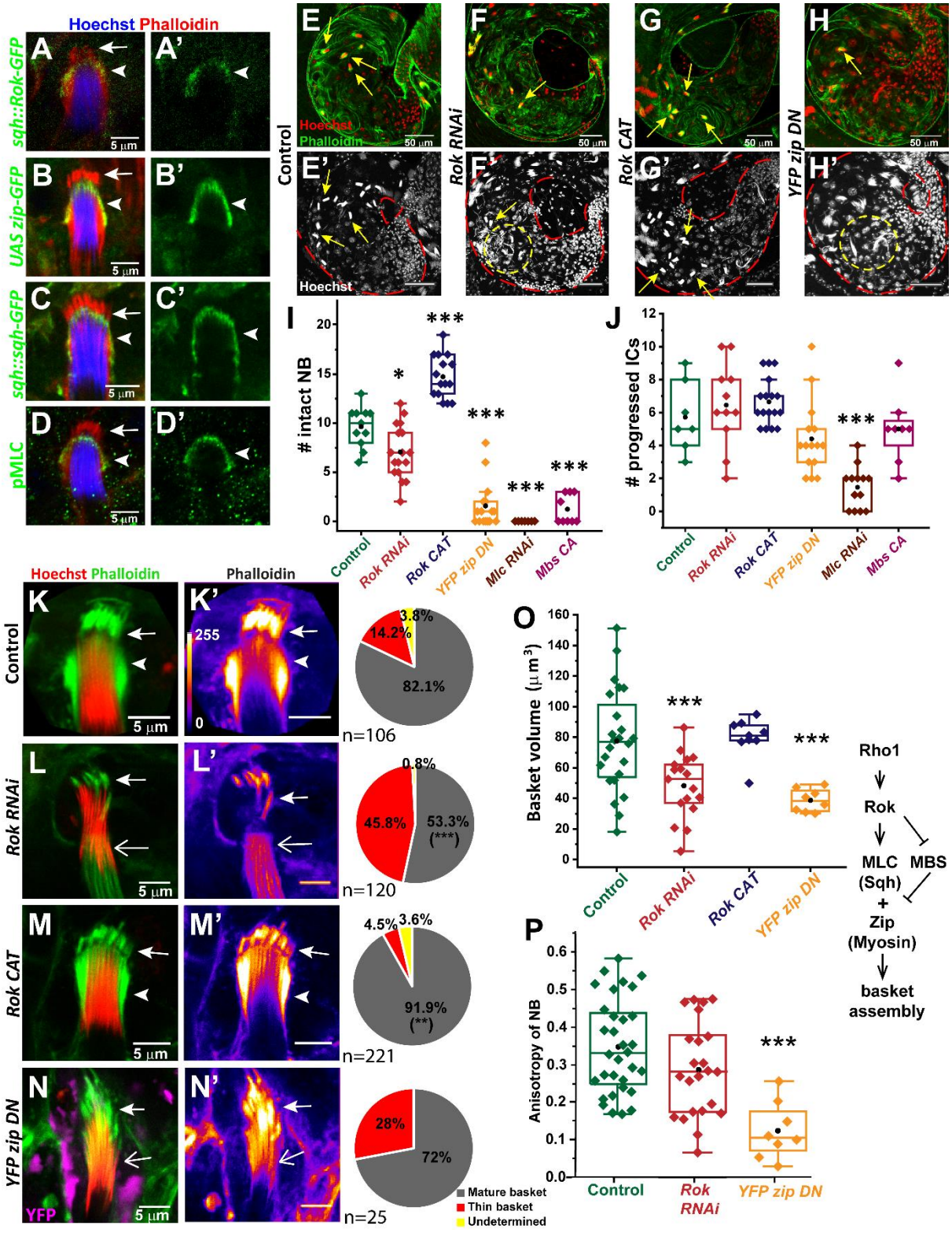

Figure 6- Rok and nonmuscle myosin-II (NM2/Zipper) function is essential for the basket assembly.

A-D) NB from testes expressing (green) *Sqh*::*Rok-GFP* (A-A'), *PpY>zip-GFP* (B-B'), *sqh::sqh-GFP* (C-C'), and stained with anti-pMLC (D-D'), respectively, along with Hoechst dye (blue) and Phalloidin (red).

781 Note that the localisation pattern is restricted to the basket (arrowheads) domain, and is absent from
782 the caplets (arrows).

783 **E-H)** TE regions of Control (E-E'), *PpY>Rok RNAi* (F-F'), *PpY> Rok-CAT* (G-G'), and *PpY>YFP-zip DN* (H-H')
784 testes, stained with Hoechst (red/ white), and Phalloidin (green).

785 **I-J)** Box plots depict the number of intact NBs (I) and the number of progressed ICs (J) in different
786 genetic backgrounds. The pairwise significance of difference with respect to the control value was
787 estimated using Mann-Whitney U tests, and the p-values- * <0.05, ** <0.01, *** < 0.001 are indicated
788 on each box.

789 **K-N)** High magnification images depict the morphology of the actin cap in Control (K-K'), *Rok RNAi* (L-
790 L'), *Rok CAT* (M-M') and *YFP-zip DN* (N-N') backgrounds, stained with Hoechst (red) and Phalloidin
791 (green/FIRE). Arrows indicate the caplet, arrowheads indicate basket, and the open arrow indicates
792 the actin sleeves around the spermatids. The F-actin levels are shown in false colour (K'-N') intensity
793 heat map according to the LUT on K'. Pie charts depict the frequency of different basket phenotypes.
794 The significance was calculated using the Fisher's exact test, and the p-values- * <0.05, ** <0.01, ***
795 < 0.001 are indicated on each box.

796 **O-P)** Box plots depict the volume of the basket domain (O) and the organisation (Anisotropy) of the
797 spermatid head alignment in NBs (P) in the Control, *Rok RNAi* and *YFP-zip DN* testes, respectively.
798 Significance was calculated using One-way Anova®, and the p-values- * <0.05, ** <0.01, *** < 0.001
799 are indicated on each box.

800

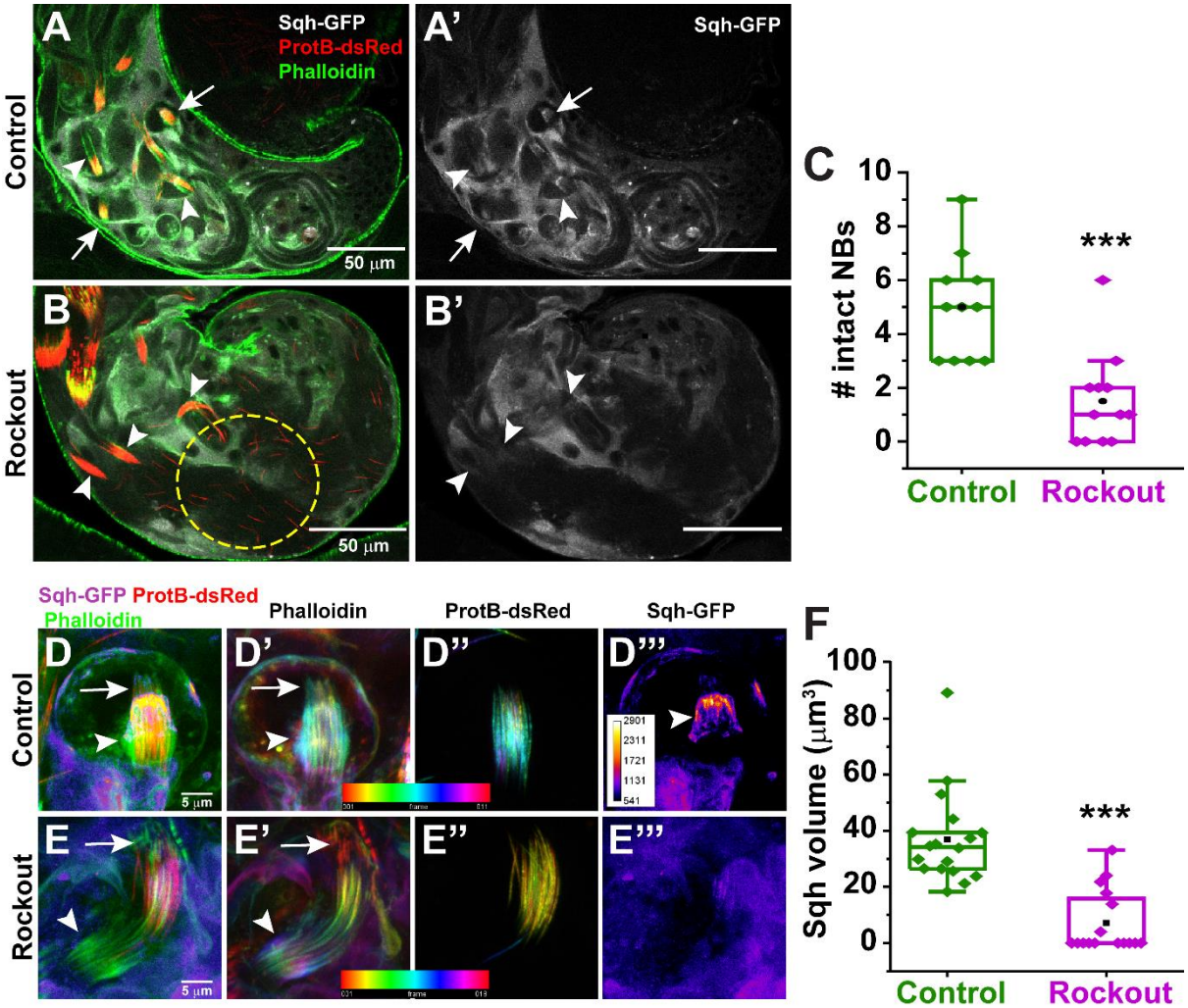
A
Sqh-GFP
ProtB-dsRed
Phalloidin
A'
Sqh-GFP
Control
50 µm
B
B'
Rockout
50 µm
C
intact NBs
***
Control
Rockout
Sqh-GFP ProtB-dsRed
Phalloidin
Phalloidin
ProtB-dsRed
Sqh-GFP
D
D'
D''
D'''
Control
5 µm
E
E'
E''
E'''
Rockout
5 µm
F
Sqh volume (µm³)
***
Control
Rockout

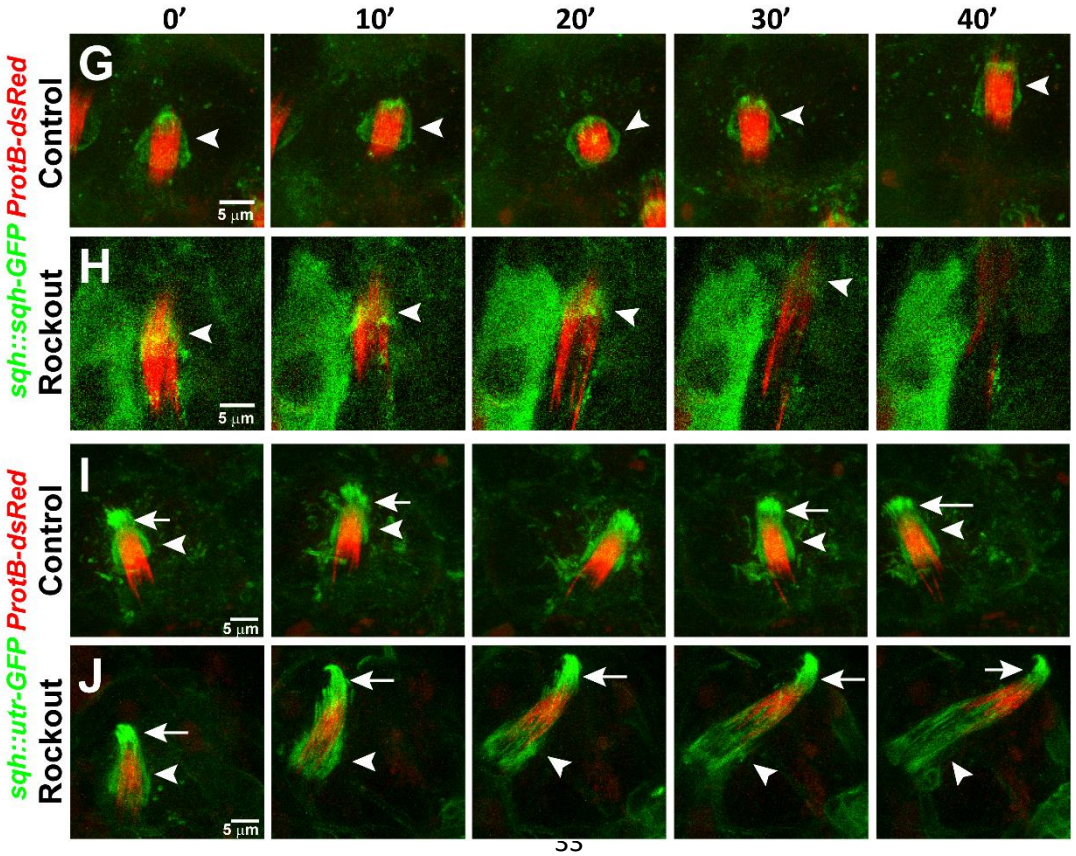
0'
10'
20'
30'
40'
G
Control
ProtB-dsRed
5 µm
H
Rockout
sqh::sqh-GFP
5 µm
I
Control
ProtB-dsRed
5 µm
J
Rockout
sqh::utr-GFP
5 µm

801

802 **Figure 7- Rok-dependent NM2 recruitment at the basket is essential for compacting the spermatid**
803 **heads into a tight bundle.**

804 **A-B)** Confocal images from *sqh::sqh-GFP* (white) and *ProtB-dsRed* (red) expressing testes, treated with
805 2% DMSO (Control, A-A') and 200 µM Rockout (B-B'), for one hour and stained with Phalloidin (green).
806 Arrows mark intact bundles, arrowheads mark bundles which have been perturbed by DMSO/ Rockout
807 treatment. Yellow dashed circle marks the disrupted sperm heads.

808 **C**) The number of intact NBs in control and Rockout treated testes. Pair-wise significance of difference
809 was estimated using Mann-Whitney U test, and the p-values- * <0.05, ** <0.01, *** < 0.001 are
810 indicated on the box.

811 **D-E)** High magnification images of NBs from Control (D-D''') and Rockout treated testes (E-E'''). D, E
812 represents the merged images, depicting Sqh-GFP (FIRE), ProtB-dsRed (red) and Phalloidin (green).
813 Arrows mark caplet, and arrowhead marks basket. D-D'' and E-E'' represent depth coded Z-stack for
814 Phalloidin (D', E') and ProtB-dsRed (D'', E'') in Control (D'-D'') and Rockout treated (E'-E'') testes,
815 respectively. The colour code is according to the scale depicted in the images. The Fire LUT (E''')
816 represents the intensity heat map.

817 **F)** Basket volume marked by Sqh-GFP in Control and Rockout treatment testes. Significance was
818 calculated using Mann-Whitney U test, and the p-values- * <0.05, ** <0.01, *** < 0.001 are indicated
819 on the box.

820 **G-J)** Time-lapse images of testes expressing *sqh::sqh-GFP* and *ProtB-dsRed* (G, H), and *sqh::utr-GFP*
821 and *ProtB-dsRed* (I, J), respectively, after the DMSO (Control) and Rockout treatments. The arrows
822 indicate caplet and the arrowheads indicate the basket domains.

823

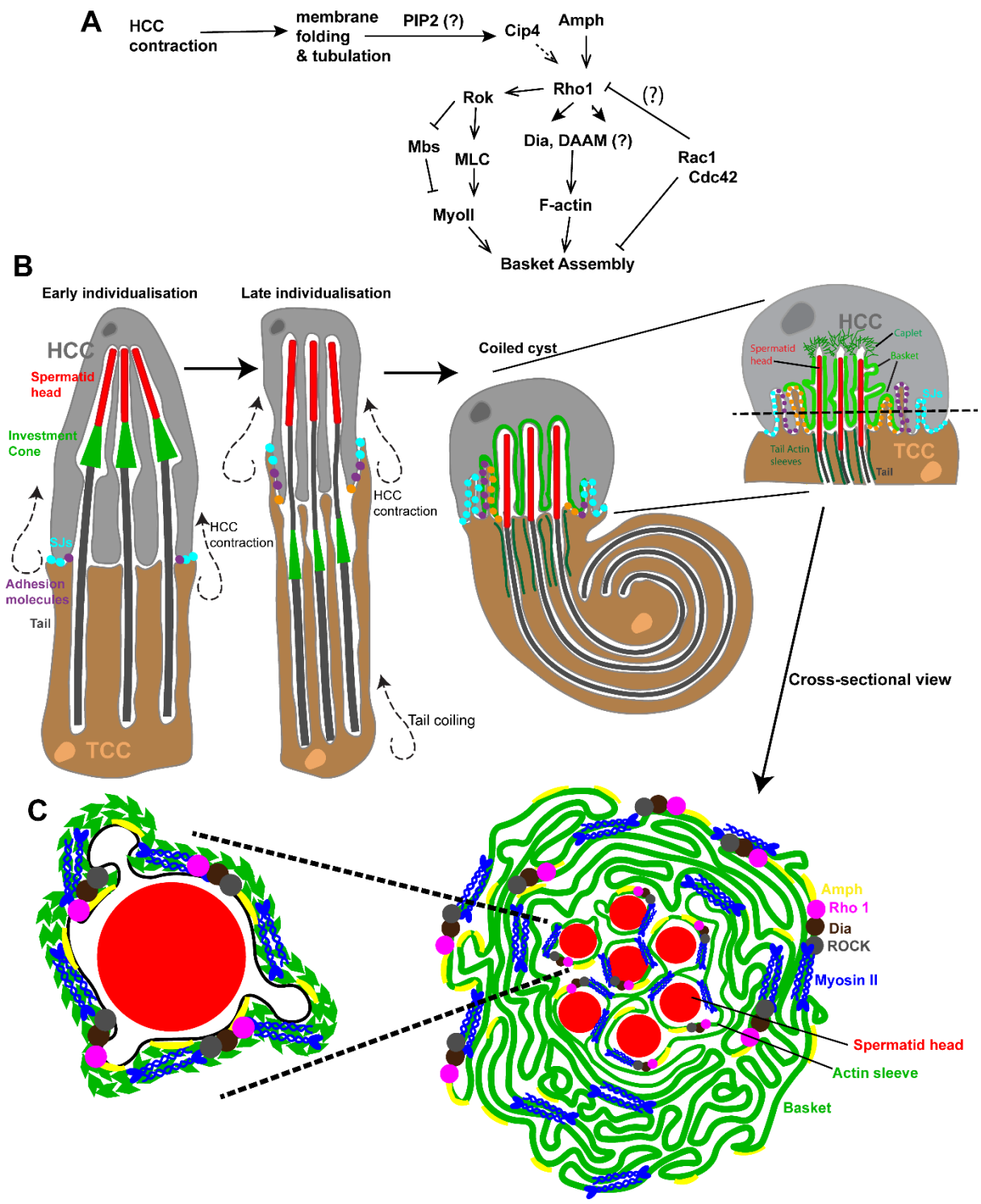

824

825 **Figure 8- Assembly of the contractile actomyosin scaffold around mature spermatid heads butting**
826 **into the somatic head cyst cell.**

827 Flow chart and schematic depict how remodelling of the membrane during individualisation to coiling
828 transition of the cyst, can potentially recruit Amph, which may intern recruit Rho 1. Rho 1 forms the
829 basket and maintains NB arrangement, via the activation of the formins, Dia and DAAM, and the Rho

830 kinase Rok, which in turn activates NM-2. (Refer to Fig. 1E for cross-section morphology depicted in
831 C)